Ph.D. DISSERTATION

PROGRAMMABLE WRINKLE PATTERNING ON MICROPARTICLES

미세입자 기반의 조절 가능한 주름 패턴 형성 기법

BY

HYUNG JONG BAE

FEBRUARY 2017

DEPARTMENT OF ELECTRICAL ENGINEERING AND
COMPUTER SCIENCE
COLLEGE OF ENGINEERING
SEOUL NATIONAL UNIVERSITY

Ph.D. DISSERTATION

PROGRAMMABLE WRINKLE PATTERNING ON MICROPARTICLES

미세입자 기반의 조절 가능한 주름 패턴 형성 기법

BY

HYUNG JONG BAE

FEBRUARY 2017

DEPARTMENT OF ELECTRICAL ENGINEERING AND
COMPUTER SCIENCE
COLLEGE OF ENGINEERING
SEOUL NATIONAL UNIVERSITY

PROGRAMMABLE WRINKLE PATTERNING ON MICROPARTICLES

미세입자 기반의 조절 가능한 주름 패턴 형성 기법

지도교수 권 성 훈

이 논문을 공학박사 학위논문으로 제출함

2017 년 2 월

서울대학교 대학원

전기컴퓨터 공학부

배 형 종

배형종의 공학박사 학위논문을 인준함

2017 년 2 월

위 원 장 : ________박 영 준________

부위원장 : ________권 성 훈________

위 원 : ________김 성 재________

위 원 : ________선 정 윤________

위 원 : ________박 욱________

Abstract

Wrinkles can be defined as sinusoidal topography with ridge and valley structures, and they commonly exist in various organisms like human skins. Many scientists have studied to understand the fundamental principles of the natural wrinkling phenomenon in various material systems. Moreover, engineers have also paid attention to these spontaneously generated wrinkle patterns found in nature, even with complex structures in micro/nano scale, because it is hard to fabricate them with conventional lithography technologies. Therefore, various bottom-up patterning methods based on the mechanical instability have been developed as alternatives to top-down patterning approaches.

To utilize wrinkling as patterning purposes, appropriate control mechanisms are required in the fabrication processes due to the random nature of it. Although numerous patterning technologies with controllability have been developed by pre-patterning the substrates or films, engineering the stress states, and others, it was elusive to achieve both the flexible pattern design (e.g., precise control of in individual ridge to any geometry) and the high-throughput production of heterogeneously patterned structures, simultaneously. In this dissertation, a new wrinkle patterning platform based on the microparticle substrate is presented, which is able to realize them and thus to extend utility of the wrinkle patterns.

For this purpose, polymeric microparticles coated with silica film were utilized for the unit structure, because the parameters to program the resulting wrinkle patterns (e.g., elastic modulus, film thickness, and geometry of the microparticle) could be dynamically tuned in each microparticle during the fabrication processes. By shrinking the homogeneously or heterogeneously programmed silica-coated microparticles, a few thousands of wrinkled microstructures could be constructed in a single fabrication process.

First, the random wrinkle patterns were generated on plane, disk-type microparticles, and they were utilized as unclonable codes analogous to human fingerprint for anti-counterfeiting purposes. Using conventional fingerprint identification algorithms, the authentication system of these artificial fingerprints was demonstrated, and the uniqueness, individuality, and durability of them were verified. This application was the first functionalization of random wrinkle patterns.

Next, several control techniques were applied to tune the degree of the pattern randomness or the directionality of ridges in low-level. Further, an elaborate wrinkle control mechanism was developed by pre-patterning the ridge guiding structures consisting of small grooves on the surface of the polymeric microparticles. This slightly modified patterning method allowed the self-organization of microstructures with precise control of the individual ridge orientation over the randomness. Not only the anisotropic, orthogonal, and hexagonal ridge patterns, but also the letter-shaped ridge patterns were realized.

Although this dissertation focused on the polymeric microparticles covered by silica, the presented programmable wrinkle patterning concept could be also applied to other materials or substrates systems. It is expected that this patterning technology and the resulting structures could be utilized for various purposes other than the presented applications, including those for useful experimental platforms in studying mechanical instability.

Keywords: Wrinkle patterning, Wrinkle control, Microparticle, Anti-counterfeiting, Self-organization

Student Number: 2013-30238

Contents

Abstract in Korean

List of Figures

List of Tables

Chapter 1

Introduction

In this chapter, the wrinkling phenomenon in a general two-layer system and the related basic theory will be briefly explained. The previously studied wrinkle patterning technologies on planar and curved substrates will then be reviewed with their various applications. Finally, the idea of a new wrinkle patterning method on the microparticle-based substrate and main claims of this dissertation will be presented.

1.1 Principle of Wrinkling

Wrinkles are frequently found in nature, for example, in human or animal skins, fruit peels, and leaves of plants. To understand the underlying principle of wrinkling, many scientists have studied the mathematics of buckling in two-layer systems and have established basic theoretical models for them [1]-[5].

When a compressive force is applied on the bilayer structure consisting of a hard thin film on a soft substrate, surface wrinkles are formed if the force exceeds a critical value. The compressive force can result from various mismatched deformations between the film and the substrate, including differential growth, thermal expansion mismatching, swelling or dehydration mismatching, and osmotic pressure [6]. According to the theoretical studies [1, 2, 7], if we assume that the shear stress between the film (f) and the substrate (s) is negligible, and consider only the elastic moduli (E_s and E_f) and the Poisson's ratios (ν_s and ν_f), the compressive force on the skin is expressed by

$$F = E_f \left[\left(\frac{\pi}{\lambda} \right)^2 \frac{wt^3}{3\left(1-\nu_f^2\right)} + \frac{\lambda}{\pi} \frac{E_s w}{4\left(1-\nu_s^2\right) E_f} \right] \tag{1.1}$$

where t is the film thickness, w is the film width, and λ is the wavelength of the wrinkle pattern along the applied compressive force direction (Figure 1.1). Wrinkling only occurs when this compressive force is larger than the critical value, F_c. The corresponding critical wavelength is then expressed by

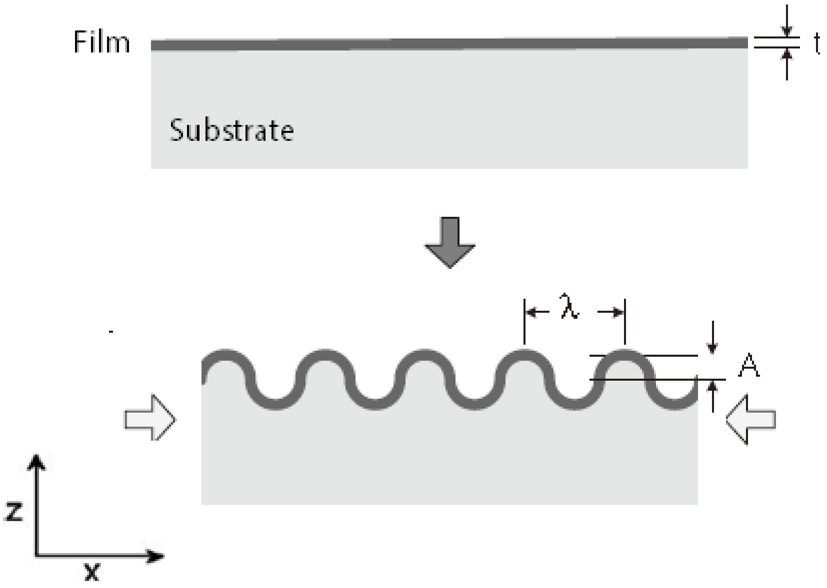

Figure 1.1 Schematic illustration of wrinkling by compressive stress in a bilayer system [8].

$$\lambda_c = 2\pi t\left[\frac{\left(1-\nu_s^2\right)E_f}{3\left(1-\nu_f^2\right)E_s}\right]^{1/3} \tag{1.2}$$

when ($\mathrm{d}F/\mathrm{d}\lambda$) = 0. Also, the amplitude, A, generally satisfies the following relation

$$A \sim \lambda\left(\frac{\Delta}{W}\right)^{1/2} \tag{1.3}$$

where Δ/W is an imposed compressive strain [4].

The equation (1.2) reveals that the wavelength of the wrinkle pattern is determined by the material properties of the film and the substrate, and the thickness of the film. Therefore, the engineering of wrinkle patterns have conventionally been achieved by changing the combination of materials, the elastic modulus in a fixed material, or the thickness of the film. In this dissertation, the wavelength will be focused on as an engineering parameter rather than the amplitude of the wrinkle pattern.

The morphology of wrinkle patterns is determined by the ratio of the two stress values in x and y directions on the plane (e.g., uniaxial or biaxial stress) and by the ratio of the applied stress to the critical stress value. Specifically, the anisotropic and the herringbone or random (labyrinth) patterns are generated by the uniaxial and equibiaxial stress, respectively, at the high overstress condition. On the contrary, the dimple or bump patterns are generated at the low overstress conditions [9].

1.2 Wrinkle Patterning Methods

Patterning technologies of nano- and microstructures based on various lithographic techniques have received significant attention in various fields including optics, biology, and material sciences because of the value of engineered substrates. However, these top-down based processes usually have limitations in terms of cost, pattern resolution, and compatibility with various materials. Therefore, the bottom-up fabrication processes have become significantly important because of their high scalability and inexpensive fabrication costs compared to the top-down processes. Among various bottom-up approaches, mechanical instability, particularly wrinkling, has been widely utilized in order to fabricate periodic patterns in large areas with low cost since N. Bowden et al. pioneered this field. In this section, some representative research about engineering wrinkles with controllability will be selectively reviewed according to the substrate geometry.

1.2.1 Planar Substrates

Most wrinkle patterning studies have been performed using planar substrates. According to the control mechanism, previous research can be classified into four categories; i) pre-patterning of substrates or films, ii) control of stress states, iii) direct wrinkle patterning, and iv) others.

First, a number of research work has achieved controlled wrinkle patterns by pre-patterning the substrate or film with specific structures. N. Bowden et al. fabricated ordered wrinkle patterns by pre-patterning polydimethylsiloxane (PDMS) substrates with bas-relief structures [10]. After heating the patterned PDMS substrate, they deposited metal film onto it and cooled it down to induce spontaneous buckling. Consequently, ordered wave patterns were generated on the surface between the elevated structures (Figure 1.2(a)). N. Bowden et al. also demonstrated aligned wrinkles using similar bas-relief structures (Figure 1.2(b)).

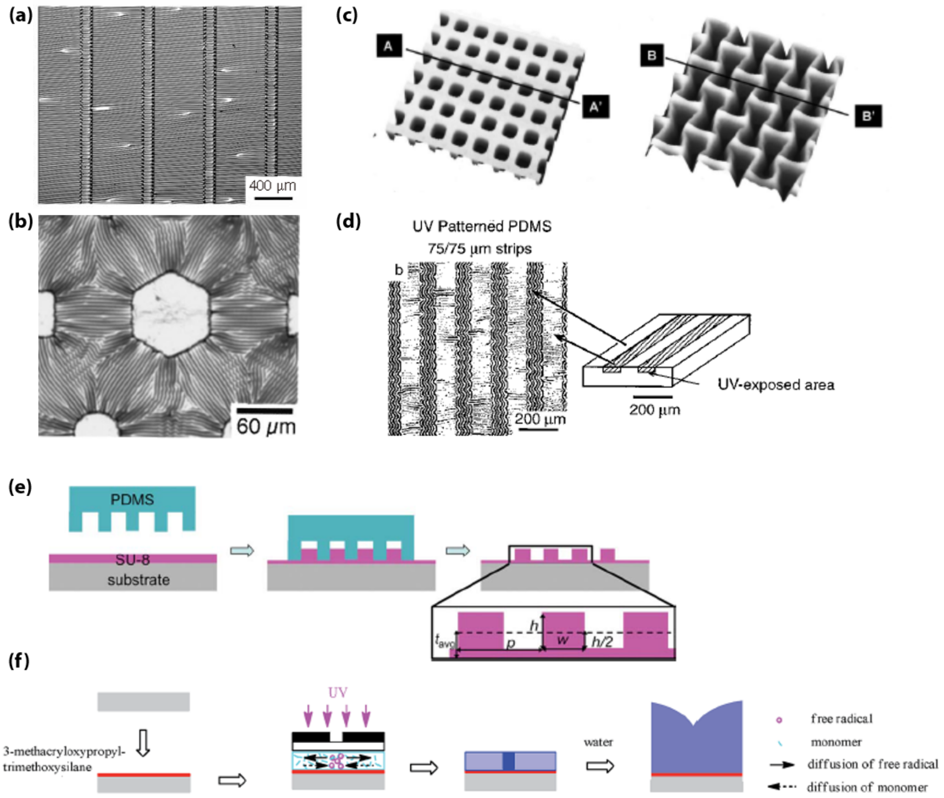

Figure 1.2 Examples of controlled patterning through pre-patterning of substrates or films: (a-c) Pre-patterning substrates with bas-relief structures [10], [11], [12]; (d) Modification of a substrate surface with different elastic modulus [13]; Pre-patterning films using (e) templates [14] or (f) photolithography [15].

However, they utilized different film material (silica by oxidizing the PDMS surface) in order to obtain a shorter wavelength [11]. After this pioneering work, various techniques were developed. D. B. H. Chua et al. fabricated ordered periodic structures by exposing the PDMS substrate pre-patterned with grooves to oxygen plasma (Figure 1.2(c)) [12]. W. T. S. Huck et al. achieved differently ordered wrinkle patterns by selectively modifying the PDMS surface before depositing the metal film [13]. The modified and the unmodified areas then presented different directionalities of wrinkles (Figure 1.2(d)). C.-M. Chen et al. pre-patterned one-dimensional (1D) structures on SU-8 film by capillary imprint lithography (Figure 1.2(e)). The wrinkles were generated by swelling the patterned film, and the pattern morphology was controlled by changing the pitch and height of the 1D pre-pattern [14]. Similarly, Q. Du et al. controlled patterns by swelling the pre-patterned hydrogel films (Figure 1.2(f)) [15].

Second, in order to tune the directionality of wrinkles, the compressive stress was controlled by using mechanical clamps. P.-C. Lin and S. Yang fabricated uniformly ordered herringbone structures by sequentially stretching and releasing the PDMS along each axis [16]. The simultaneously stretched and released substrate showed rather random wrinkle patterns due to equibiaxial stress (Figure 1.3(a)). C.-C. Fu et al. also controlled the release of stress in order to obtain biaxial and uniaxial wrinkle patterns (Figure 1.3(b)) [17]. Similarly, E. Lee et al. fabricated anisotropic

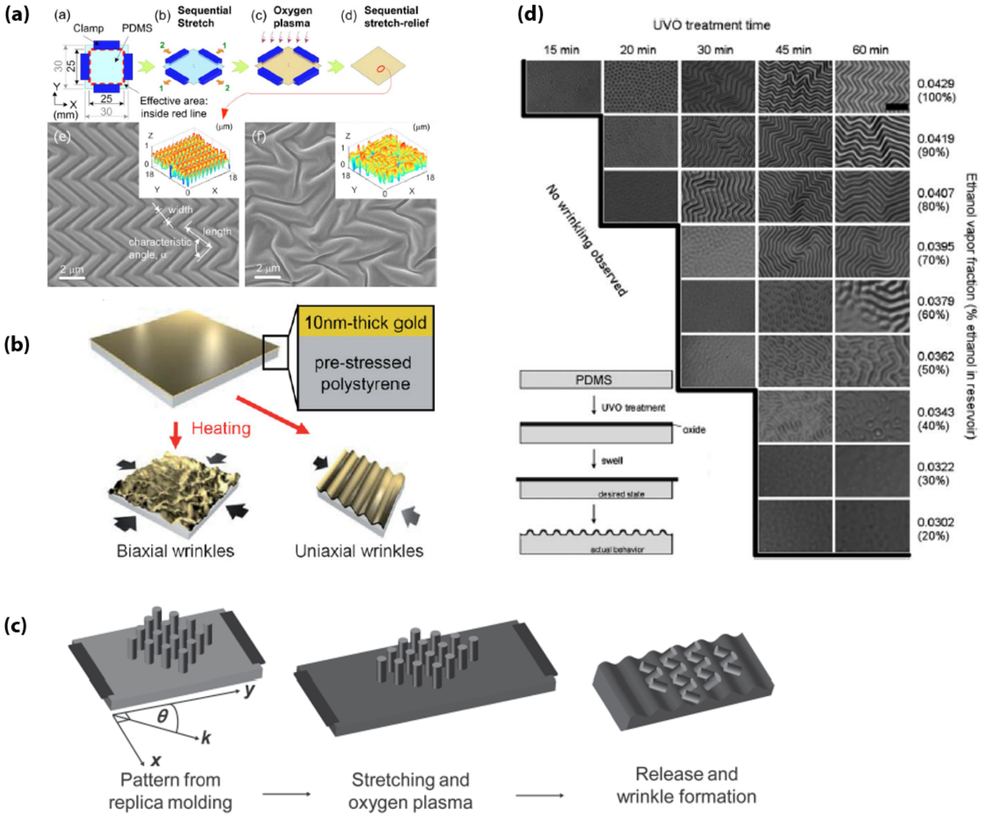

Figure 1.3 Examples of controlled patterning by regulating stress states: (a) Control the stretching and releasing of the prestress in sequential manner [16]; (b-c) Control the prestress state biaxially or uniaxially [17], [18]; (d) Control the magnitude of the applied stress [9].

PDMS wrinkles using the same method in order to control the tilting angles of pillar arrays atop the wrinkled substrate for optical applications (Figure 1.3(c)) [18]. In addition, D. Breid and A. J. Crosby controlled wrinkle morphologies by manipulating the magnitude of applied stress in both equibiaxial and non-equibiaxial stress states [9]. They applied swelling stress on the thin films fabricated by the UV-ozone oxidation of PDMS substrates. The magnitude of the stress was controlled by changing the UV-ozone treatment time and the concentration of solvent vapor. They achieved a morphology transition from the dimple to the herringbone or random patterns as the overstress (applied stress above the critical buckling stress) increased (Figure 1.3(d)). Although these pre-patterning or stress control techniques allowed the ordering of ridge orientation in the overall pattern, they could not provide the precise control of individual ridges in specific regions.

On the contrary, some research demonstrated more flexible patterning by directly generating ridges on the substrate. For example, M.-W. Moon et al. irradiated a focused ion beam (FIB) on the PDMS sheet to selectively generate wrinkles on the exposed area [19]. They controlled the pattern morphology by changing the relative velocity between the beam and the PDMS sheet, the ion beam spot diameter, the ion beam spot spacing, or the ion beam fluences (Figure 1.4(a)). C. F. Guo et al. utilized a laser with a gold/polystyrene bilayer system in order to precisely control the location and geometry of wrinkle patterns [20]. They locally

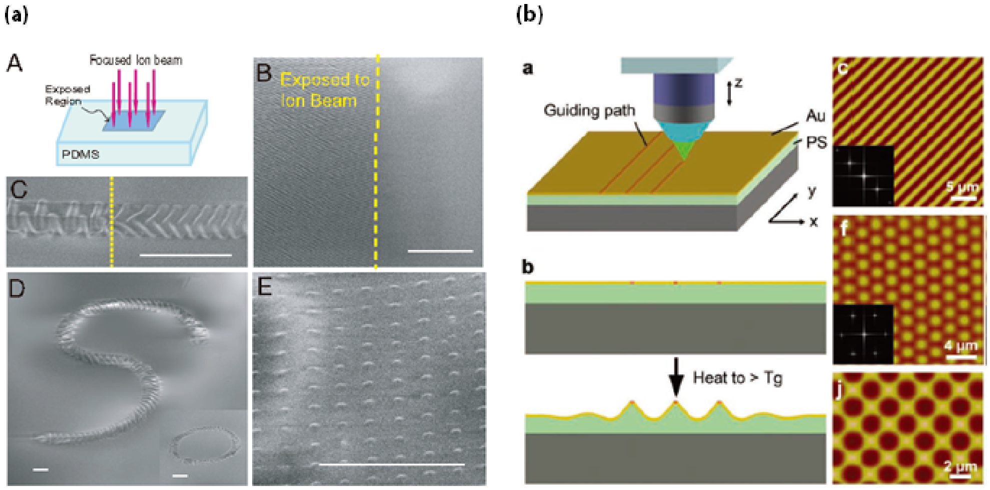

Figure 1.4 Representative direct wrinkle patterning methods: (a) Creating spatially controlled wrinkles with FIB irradiation [19]; (b) Path-guided wrinkling with laser direct writing method [20].

modified the elastic modulus of the gold film using a laser whose feature size was smaller than the wavelength scale. These modified regions then served as a guiding path and they became ridges under the heating condition. Various wrinkle patterns were demonstrated using this method (Figure 1.4(b)). Although these direct wrinkle patterning approaches successfully achieved diverse patterning with controllability compared to the previous control mechanisms, they also have limitations in scalability and throughput, because they cannot utilize the bottom-up nature of wrinkling in bulk scale.

In addition to these methods, various wrinkle patterning methods were developed with different material systems. P. J. Yoo et al. utilized external mold in order to guide surface wrinkles and fabricated anisotropic patterns (Figure 1.5(a)) [21, 22]. M. Guvendiren et al. utilized elastic modulus gradients of hydrogel film and the corresponding change of osmotic pressure under the swelling process, in order to control wrinkle morphologies (Figure 1.5(b)) [23]. S. J. Ma et al. selectively patterned wrinkles by illuminating UV light with photomasks (second polymerization) on the pre-stretched polymer network (first polymerization) [24]. The ordered wrinkle patterns were then fabricated only on the UV exposed region (Figure 1.5(c)). However, these patterning methods also lacked the ridge orientation control mechanisms independently applicable at the individual ridge level throughout the entire pattern region.

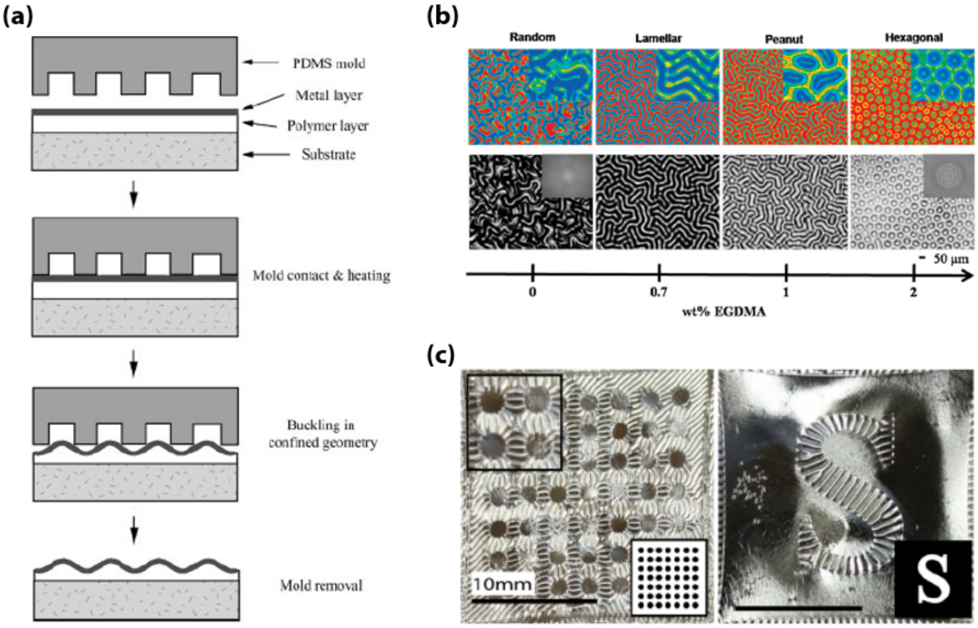

Figure 1.5 Other various wrinkle patterning techniques: (a) Guiding of wrinkles using a mold [21]; (b) Morphology control using elastic modulus gradient of films [23]; (c) Spatially controlled patterning using two-stage polymerization [24].

1.2.2 Curved Substrates

Studies about mechanical instability in curved substrates have not received sufficient attention compared to those in planar substrates. Specifically, although theoretical studies (including numerical simulations) were performed by many scientists [6], [25]-[27], experimental platforms for verifying the simulation results or for investigating parameters on curved substrates (e.g., curvature) were lacking. Here, several experimental demonstrations for studying the buckling phenomenon on various three-dimensional (3D) structures are briefly introduced.

G. Cao and X. Chen studied the effect of curvature on spherical substrates [28]. Using a spherical Ag core/SiO_2 shell microparticle, they experimentally verified the relationship between the morphology of wrinkle patterns and the curvature or the film stress (Figure 1.6(a)). J. Yin et al. studied spontaneous buckling patterns in disk-type microstructures both analytically and experimentally [29]. They demonstrated the fabrication of various kinds of cylindrical gears by controlling the geometry and the elastic modulus of the substrate and film (Figure 1.6(b)). A. C. Trindade et al. presented Janus particles by partially generating random wrinkle patterns on one half of an elastomeric sphere [30]. They controlled the pattern wavelength by changing the thickness of the shell, the particle diameter, and degree of swelling (Figure 1.6(c)). D. Breid and A. J. Crosby also investigated the effect of the radius of curvature on wrinkle morphology in spherical PDMS surfaces [31]. They found that wrinkle morphology changed from hexagonal dimples to long ridge patterns as the radius of the curved substrate increased (Figure 1.6(d)). They also experimentally examined the effect of the film thickness and applied swelling stress at a constant radius. Most recently, M. Li et al. developed a fabrication method for wrinkled 3D structures with various shapes [32]. By controlling the polymer monomer concentration with UV exposure time at the photopolymerization step for 3D post construction, they tuned the wavelength of wrinkle patterns on the base and post surfaces (Figure 1.6(e)).

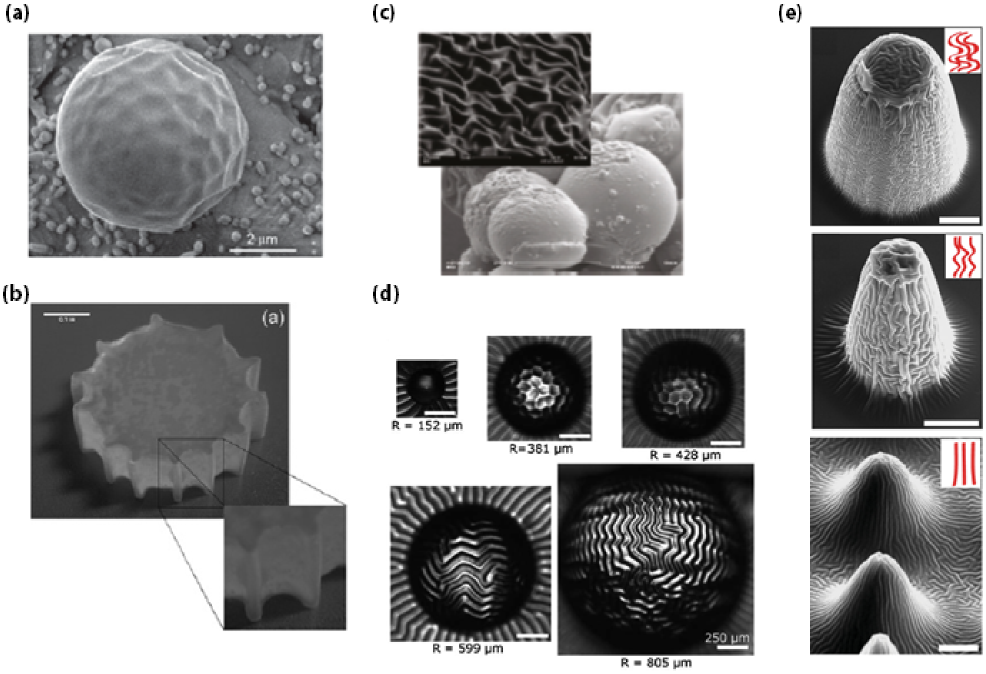

Figure 1.6 Studies of wrinkling on curved substrates: (a) The effect of substrate curvature and the film stress in a microparticle [28]; (b) Wrinkling in cylindrical structures [29]; (c) Partial wrinkling in spherical particles [30]; (d) The morphology change in a spherical PDMS substrate [31]; (e) Wrinkle patterning on 3D posts [32].

1.3 Applications

Spontaneously generated wrinkle patterns have been widely utilized for various purposes due to their useful function. Some representative applications of wrinkle patterns or wrinkling phenomenon were selected and summarized in Table 1.1.

In biology, the unidirectionally ordered wrinkle patterns can be utilized as a cell culture environment, providing mechanical or topographical cues to cells. Therefore, these patterns were applied to analyze cell morphology [33] or to control the differentiation of stem cells based on the wrinkle morphology [34, 35]. Also, the highly periodic wrinkle patterns are useful in optics including optical gratings [36] or microlens arrays [37]. The characteristic wavelength of wrinkle patterns in soft material films can be used to extract elastic modulus from the film material, which is difficult to obtain using the conventional nanoindentation method [38]. Moreover, controlled wrinkle patterns can be utilized to fabricate microfluidic channels [39], to print small molecules by stamping with wrinkled structures [40], or to prevent the fouling of marine organisms [41]. Meanwhile, random wrinkle patterns can also be applied to enhance adhesion of the surface [42]. In addition to wrinkle patterns, the buckling concept has been widely adopted for fabricating conformal devices in the flexible or stretchable electronics field [43, 44].

Table 1.1 Various applications of wrinkle patterns

Application		Control method	References
Biology	Cell guidance	Stress state control	[33]
	Stem cell control	Stress state control	[34], [35]
Optics	Phase grating	Stress state control	[36]
	Microlens	Pre-patterning film	[37]
Metrology		Stress state control	[38]
Microfluidics		Stress state control	[39]
Microcontact printing		Stress state control	[40]
Anti-fouling		Stress state control & Pre-patterning film	[41]
Adhesive		-	[42]
Stretchable electronics		-	[43], [44]

1.4 Main Concept: Wrinkle Patterning on Microparticles

As examined in previous sections, most wrinkle patterning technologies and their applications were focused on two-dimensional (2D) planar substrates. Although these approaches are advantageous in fabricating homogeneous wave patterns in large scale, they generally lack flexibility or diversity in pattern design due to the absence of precise ridge control mechanisms, or have limited fabrication throughput in fabricating a number of heterogeneous structures. In this dissertation, a new wrinkle patterning platform based on a 3D microparticle substrate is developed in order to provide a flexible design scheme and heterogeneous patterning in a high-throughput manner.

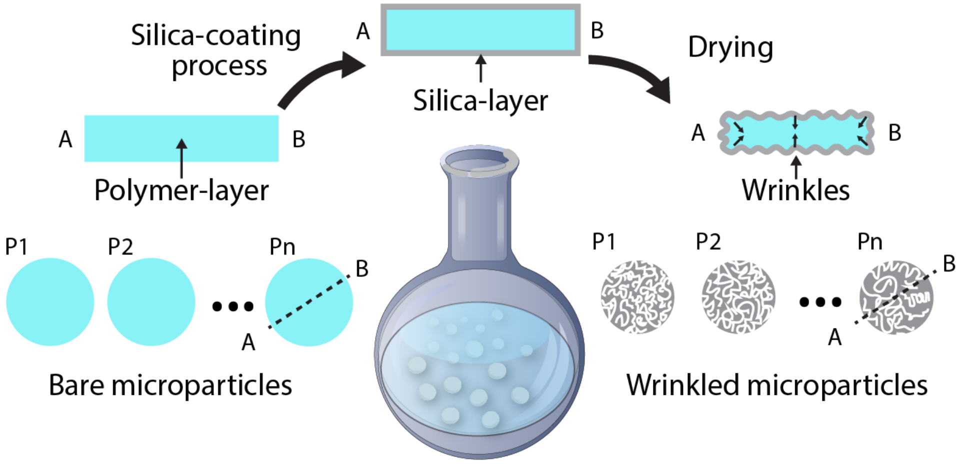

Figure 1.7 Schematic illustration of the whole process for wrinkle patterning on the microparticle-based substrate. This consists largely of two parts; the polymeric microparticle synthesis and the subsequent silica-coating and drying [45].

For this purpose, a two-layer structure with the elastic polymeric microparticle substrate and the hard silica film was constructed (Figure 1.7). This was achieved by photopolymerizing a polymer solution to microparticles with a certain shape and coating them with silica. For inducing compressive stress, the silica-coated microparticles were shrunk during the drying step. The resulting wrinkles were spontaneously generated on both the top, bottom and side surfaces (Figure 1.8). As a result, the heterogeneously patterned microstructures were able to be generated from the identical microparticles in a single batch. This platform provided a flexible pattern design strategy with high-throughput fabrication because the mechanical properties or geometry of the individual microparticles could be dynamically controlled during the fabrication process.

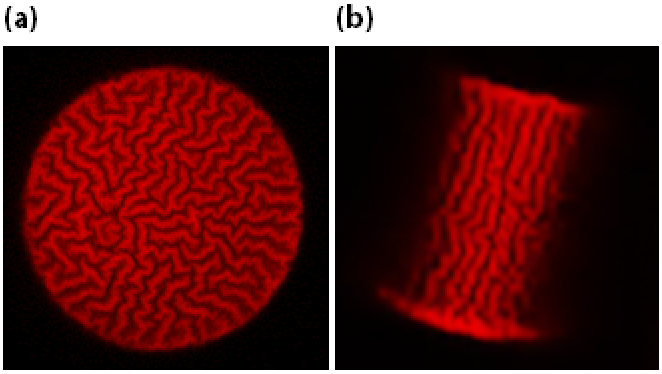

Figure 1.8 Fabricated wrinkled microparticle: (a) Confocal laser scanning microscopy (CLSM) image of the bottom surface of the particle; (b) CLSM image of curved side surface of the particle.

In chapter 2, the fabrication processes for wrinkled microparticles with random patterns will be explained in detail. In chapter 3, an advanced anti-counterfeiting microtaggant platform will be demonstrated using these wrinkled microparticles. In chapter 4, several pattern-control mechanisms will be presented by developing the random wrinkle patterning method, and I finally conclude in chapter 5.

Chapter 2

Patterning Random Wrinkles

In this chapter, a general wrinkle patterning method on a particle-based substrate is presented. First, the microparticle substrate synthesis process will be explained along with the material compositions that are required. The fabrication process of the shell layer for constructing a bilayer system will then be described. Finally, the wrinkling process and the conditions for surface wrinkle generation will be detailed.

2.1 Microparticle Synthesis

To induce wrinkling in the microparticle, it requires two different material layers with a core−shell structure. For the core substrate, we utilized polymeric microparticles that were synthesized through photopolymerization of polymer monomers using the optofluidic maskless lithography (OFML) system that was developed by our research group [46].

First, the prepolymer mixture was prepared to a 7:3 volume ratio of trimethylolpropane ethoxylate triacrylate (ETPTA, Mn~428) and 3-(trimethoxysilyl) propyl acrylate (TMASPA) as a alkoxysilane-grafted photocurable resin with 10 vol% of the photoinitiator. Additionally, 0.025 wt% of methacryloxyethyl thiocarbamoyl rhodamineB was added to this prepolymer mixture for fluorescence imaging of the particle surface (Figure 2.1).

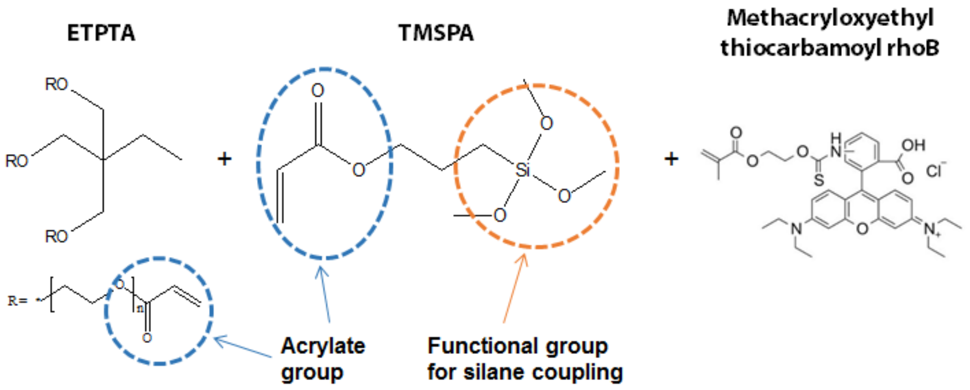

Figure 2.1 Composition of the photocurable prepolymer resin. Photoinitiator was added to this for photopolymerization.

Acrylate groups in both ETPTA and TMSPA were crosslinked by the ultraviolet (UV) light illumination, resulting in polymeric microstructures. RhoB molecules were also crosslinked within the polymer network because it had an acrylate group. This is essential for stable fluorescence imaging of the microparticles, because general RhoB molecules without acrylate groups are washed out from the microparticle during the following steps after the synthesis process. TMSPA serves the functional group for silane coupling that enables silica formation on the surface of poylermic microparticles. This silica layer will be utilized as a hard shell in our core−shell structure, and the detailed methods for the silica formation will be described in the following section.

Next, microparticles with various shapes were synthesized using this prepolymer resin with the OFML system. This OFML system consists of a UV light source, a digital micromirror device (DMD), a motorized stage, and a microscope with objective lenses (Figure 2.2). The prepolymer resin was loaded between PDMS coated slide glasses, and these slides were placed on the motorized stage. In order to fabricate microparticles with a certain shape, UV light must be modified into this shape. The DMD allowed shaping of UV light by reflecting a specific part of the illuminated UV light, based on the photomask pattern loaded onto the DMD. As a result, we were able to synthesize various shapes of microparticles by dynamically changing the DMD mask with the appropriate design.

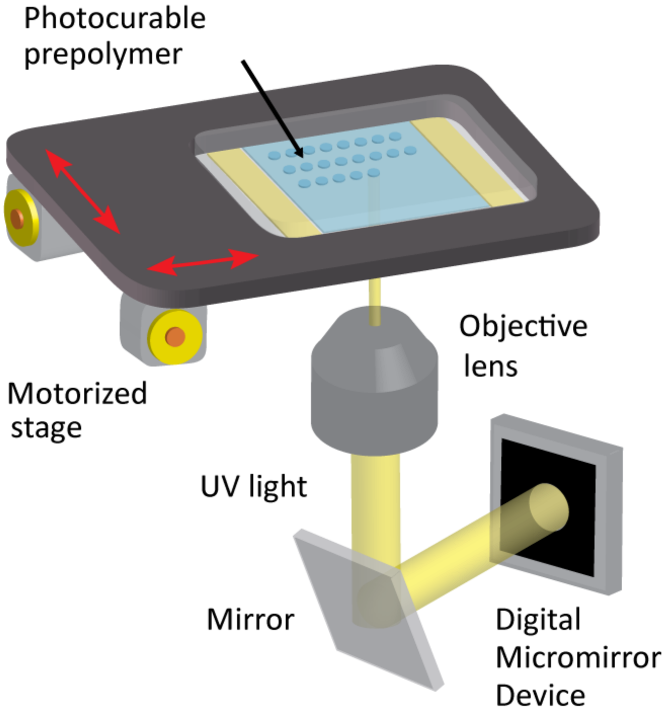

Figure 2.2 Schematic illustration of the microparticle synthesis process using the optofluidic maskless lithography (OFML) system. Ultraviolet (UV) light was directed at the prepolymer resin after being shaped by the digital micromirror device (DMD).

By synchronizing the UV light source, the DMD, and the motorized stage, we were able to automatically fabricate approximately 7,000 microparticles (100 μm size) with different shapes in a single batch. We usually used a 20x (NA 0.45) objective lens for particles less than 250 μm in size and a 10x (NA 0.3) objective lens for 250 ~ 500 μm sized microaprticles. The synthesized microparticles were washed a few times with ethanol and immersed in ethanol overnight in order to remove the uncured polymer monomers.

2.2 Silica-Coating

After synthesizing the inner substrate, we needed to fabricate the outer shell for the wrinkle patterning. For this purpose, we coated the polymeric microparticle surface with silica nanoparticles through a modified Stöber process [47, 48]. Typically, the synthesized microparticles were collected in a glass vial. Then they were immersed in a mixture consisting of ethanol (20 ml), DI water (3.2 ml), ammonium hydroxide (0.8 ml), and tetraethyl orthosilicate (TEOS, 0.1 ml), and the vial was agitated using a vortexer. Every 20 minutes, 0.1 ml of TEOS was additionally injected into the solution until the total amount of TEOS reached 0.4 ml. The microparticles were then washed two times with the same mixture solution, only lacking the TEOS. This fresh coating mixture was applied in order to prevent any shrinking of the microparticles before completing the entire coating process during the washing steps.

Next, the entire procedure was repeated until the silica-coating time reached a targeted duration [45].

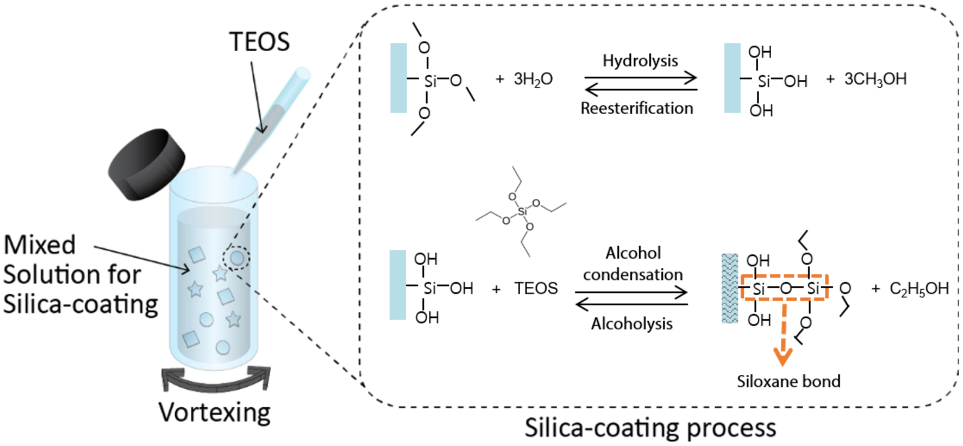

Figure 2.3 Schematic illustration of the silica-coating process. The condensation of tetraethyl orthosilicate (TEOS) on the particle surface formed a thin silica film.

Specifically, this silica-coating process is a kind of sol-gel method. The colloidal nanoparticle solution (TEOS) develops into a solid silica layer on the surface of microparticles through hydrolysis and condensation processes (Figure 2.3). Amonium hydroxide catalyzes this reaction, and its concentration affects the speed of the coating process.

Developed silica-coated microparticles can be applied for various purposes, and as an example, we demonstrated multiplex bioassays using shape-encoded silica microparticles [49]. This platform has advantages over other bead-based bioassay platforms for the following reasons; i) the encoding capacity based on graphical codes is higher than that on spectral codes, ii) the silica layer provides good physical durability, and iii) silica-based chemistries for conjugation of biomolecules are stable. Using these silica-coated microparticles, we performed multiplexed human papilloma virus (HPV) genotyping analysis (Figure 2.4). The silica surfaces were functionalized with the carboxylic acid groups by treating (3-Aminopropyl)triethoxysilane (APTES) and succinic anhydride. Then 10 different 5' amino-terminated HPV type-specific oligonucleotide probes were immobilized on the surfaces of carboxylated microparticles with 10 different shape codes, respectively. After the hybridization of biotin-labeled target HPV genes with complementary probes, R-phycoerythrin (PE)-conjugated streptavidin was added to detect fluorescent signals. Among the 10 kinds of microparticles, only those containing complementary probes for a certain target gene showed fluorescent signals. This result revealed that shape-coded silica microparticles can serve as multiplex bioassay platforms that provide high multiplexity and allow conventional chemistries for the conjugation of biomolecules, such as DNAs and proteins.

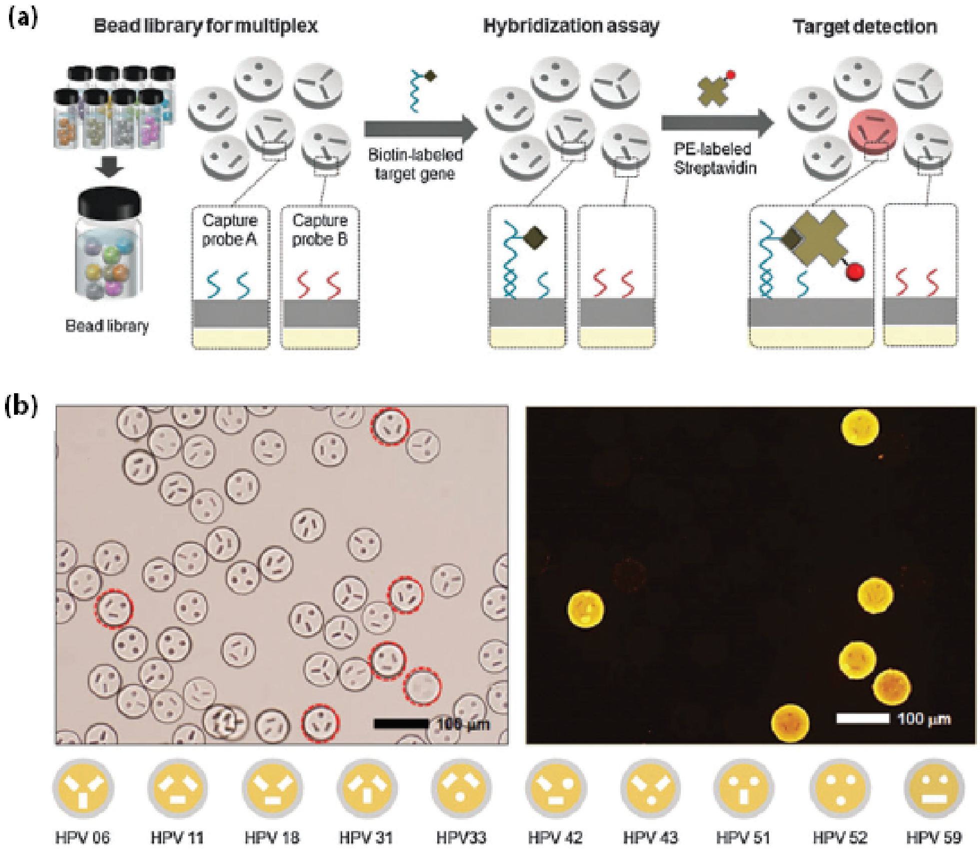

Figure 2.4 Application of encoded silica microparticles for multiplex bioassays: (a) Schematic illustration of HPV genotyping processes using silica-coated microparticles; (b) A bright-field and a fluorescent image after the hybridization assay. Only particles with probes complementary to the target HPV 33 sequences showed fluorescent signals [49].

.

2.3 Wrinkling Process

To generate wrinkles on the particle surface, we utilized shrinking of the silica-coated microparticles. Since the silica-coated microparticles consist of an elastic polymer substrate with an inelastic silica shell, the mismatched strain is induced between the shrinking core and the stiff shell when they shrink. As a result, the biaxial in-plane stress resulting from this mismatched strain spontaneously generates surface wrinkles.

In order to verify the self-organization of surface wrinkles, we observed the moment of wrinkling by continuously scanning individual microparticles using the CLSM. After the silica-coating process, the microparticles were rigorously washed with ethanol to remove debris of silica nanoparticles attached on the surfaces. Washed microparticles immersed in ethanol were then dispensed on a well in a 96-well plate. To reduce the time required for the evaporation of the solvent, we sucked out the ethanol using a pipette. A few minutes later, we observed that the edge of the evaporating solvent was moving toward the microparticle region. By setting this moment to $t = 0$, Figure 2.5 shows the evolution of surface wrinkles at intervals of five seconds. The planar bottom surface of the microparticle was transformed into a random topography through the wrinkling process. Also, we found that the particle size had been decreasing as time went by. Overall, we can conclude that random wrinkle patterns were spontaneously generated on the particle surface by the shrinkage of the microparticle through the drying process.

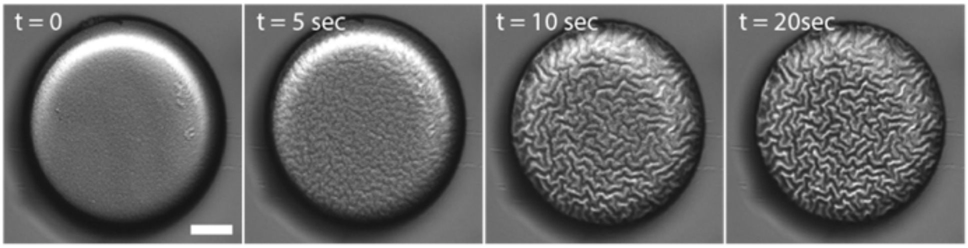

Figure 2.5 Sequence of time lapse images at the moment of wrinkling (scale bar: 25 μm) [45].

However, it is poorly understood why this labyrinth of wrinkle patterns are formed differently from one microparticle to another, and what factors govern this randomness. It seems that the resulting ridge patterns are sensitive to small geometrical perturbation on the silica-layer. The variation of the silica layer structure (e.g., local thickness deviation) in each microparticle may result in the different ridge distributions on the particle surface, even under the same wrinkling conditions [50].

We also observed the cross-section of the wrinkled surface using a scanning electron microscope (SEM). For this purpose, we prepared dry wrinkled microparticles on a carbon tape, and they were loaded into the FE-SEM device. Next, a focused ion beam was used to mill the particle surface along the z-axis after the deposition of thick platinum, for the protection of the structure. From the resulting SEM images (Figure 2.6), we were able to distinguish the polymer substrate from

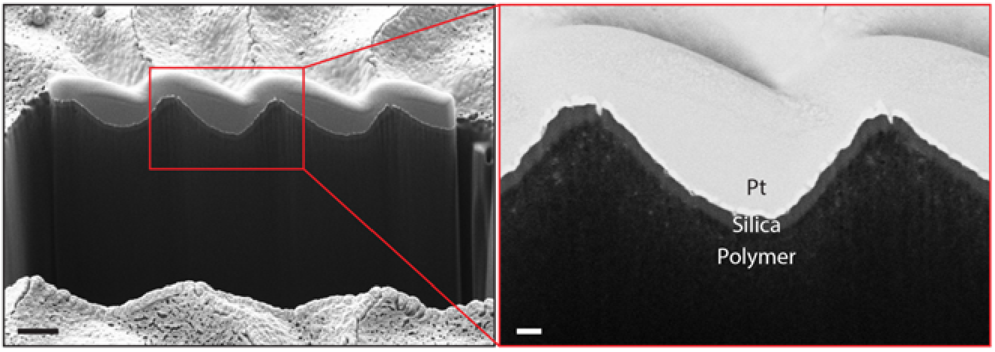

Figure 2.6 Cross-sectional view of the wrinkled microparticle (scale bar: 1 μm). In the magnified image, the silica film and the polymer substrate are distinguishable and the delamination of the silica was not observed (scale bar: 200 nm) [45].

the silica shell, and found that periodic waves were generated on the interface of the both. Also, we verified that there was no delamination of the silica layer from the polymer substrate. Moreover, we observed some cracks in ridges, which seemed to appear when the generated ridges were sharp, but did not appear when the generated ridges were smooth. However, we could not control the sharpness of the ridge shape with the current wrinkle patterning method.

To generate wrinkle patterns on the entire surface of the silica-coated microparticles through the drying process, silica nanoparticles must completely cover the particle surface during the coating process for an adequate amount of time. To verify this, we analyzed the particle surface characteristics based on the silica-coating duration (Figure 2.7). We performed random sampling of the microparticles during the silica-coating reaction at different stages (0, 40, 80, 120, 160, 240, 320, and 480 minutes after starting the coating reaction). Then, we observed the surfaces of these microparticles using a microscope. First, the wrinkles were not generated before the drying process was complete, regardless of the coating duration. Next, we dried the sampled microparticles and imaged them again. The wrinkles began to appear when the reaction time was longer than 120 minutes. To closely investigate the surface conditions, we also imaged dried microparticle samples using SEM. For up to 80 minutes of coating, the growth of the silica-nanoparticles was not enough to cover the polymer surfaces. In other words, shrinking of the particle with or without an incomplete silica shell could not generate surface wrinkles. This revealed that a complete silica layer on the polymeric microparticle is required for wrinkle patterning. Also, an excessive coating process duration resulted in unclear wrinkle patterns with large characteristic wavelengths (over 480 minutes). From this analysis, we were able to conclude that the appropriate silica coating time for wrinkle patterning ranges from 120 to 320 minutes, and thus we utilized this range for the following experiments.

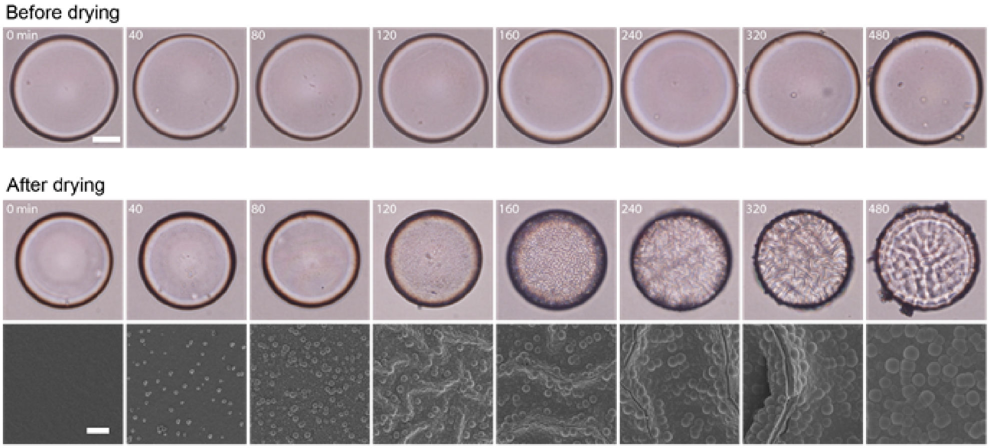

Figure 2.7 Surface characteristics before and after the drying process, depending on the silica-coating time. The bright-field images and FE-SEM images were obtained by sampling microparticles at various times during the silica-coating reaction (scale bars: 25 and 1 μm, respectively) [45].

Chapter 3

Application: Artificial Microfingerprints

In this chapter, an application of the wrinkled microparticles as microtaggants for anti-counterfeiting of products will be presented. First, counterfeit goods market trends and various efforts to prevent forgery will be briefly introduced. Second, the concept of an artificial microfingerprint will be presented using wrinkled microparticles as analogous to human fingerprints. Then, the feasibility of this artificial fingerprint for a novel unclonable microtaggant will be verified by investigating the characteristics of wrinkled microparitcles in terms of security level, code capacity, individuality of the code, and durability. Finally, the authentication process of artificial microfingerpints will be demonstrated with commercial products.

3.1 Anti-Counterfeiting Technologies

The enormous counterfeit market has been aggressively threatening markets worldwide in finance, fashion, pharmaceuticals, electronic devices, and more (Figure 3.1). Globally, the total economic value of counterfeit goods is estimated at about \$650 billion per year, and about 10% of global goods are estimated as counterfeited according to statistics. However, the real value is more likely much larger than this, because it is difficult to precisely estimate the amount of all fake products in the market. Moreover, the total value has been increasing every year. In addition to economic loss, job loss due to counterfeits is not negligible [51]. Notably, counterfeit drugs cause significant social problems because they are directly related to public health, even human life. According to statistics, 10% of medicines in the United States and 25% in developing countries are fake drugs [52]. Another statistic shows that 100,000 people die due to counterfeit drugs in Africa each year. As shown by this statistic, people in developing countries are more susceptible to counterfeits [53].

To prevent and stop counterfeiting, governments, industries, and researchers around the world have been striving to provide solutions and have been developing various anti-counterfeiting technologies. Here, as part of these efforts, we present a powerful anti-counterfeiting strategy using wrinkled microparticles. Before introducing our technology, the latest anti-counterfeiting methods will be reviewed in two different categories (taggant and physical unclonable function).

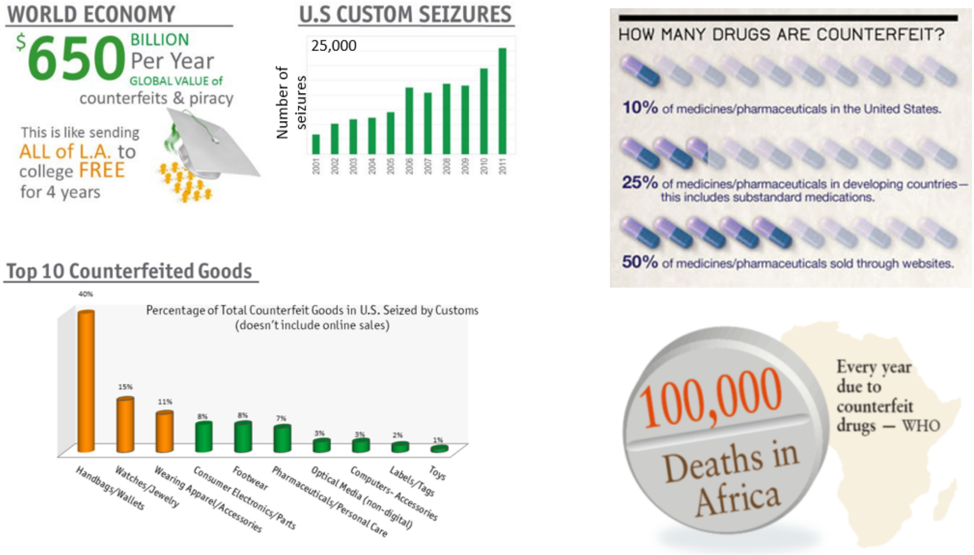

Figure 3.1 Current state of global counterfeit market and the threat of counterfeit drugs in developing countries [51]-[53].

3.1.1 Taggant Systems

A microtaggant is a microscopic and traceable particle which is added to materials or products for authentication. For example, covert microparticles with unique information can be embedded on a product surface in order to authenticate it (Figure 3.2(a), ARmark Authentication Technologies, LLC, and Colorcon, Inc.) [54]. This method is powerful because the micrometer-scale physical identifiers in the individual item cannot be easily detected, while other authentication methods such as barcode or RFID tags are more obvious.

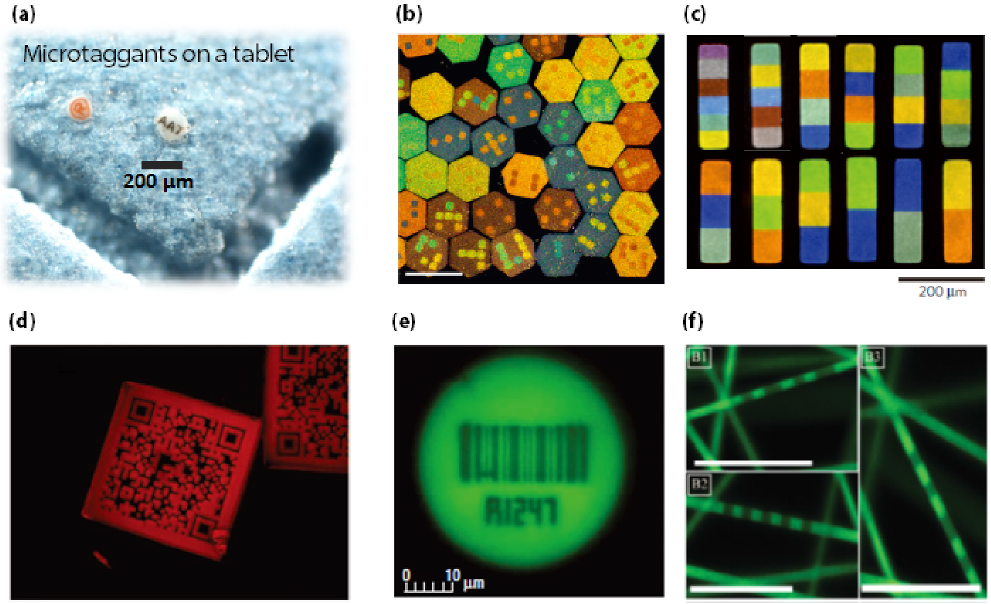

Figure 3.2 Taggant-based technologies for anti-counterfeiting purposes: (a) A commercial microtag for the drug authentication [54]; (b) Color-barcoded magnetic microparticles with structural colors [55]; (c) Color-barcoded microparticles with rare-earth upconversion nanocrystals [56]; (d) QR-coded microparticles for drug authentication [57]; (e) Encoded microcarriers by photobleaching [58]; (f) Digitally encoded microfiber for drug authentication [59].

Microtaggant encoding methods can be generally classified into two different categories; spectral encoding and graphical encoding. Fluorescent materials are usually incorporated into microparticles for spectral encoding with different emission spectrums. However, fluorescent-based encodings have critical limitations in encoding capacity, because the number of types of fluorescent dye is limited and thus cannot be applied to various products. In this context, our group developed a novel encoding method by constructing structural colors (resulting from one-dimensionally aligned superparamagnetic colloidal nanocrystal clusters) with barcode shapes (Figure 3.2(b)). Using this method, billions of different physical identifiers can be fabricated and these microparticles can be utilized as microtaggants [55]. As another approach, P. S. Doyle group developed a robust encoding method using rare-earth upconversion nanocrystals (Figure 3.2(c)). In addition to providing a large encoding capacity, they demonstrated authentication process with portable microscope devices by incorporating fabricated microtaggants on products [56].

Graphically coded microtaggants have also been widely studied, and they can provide virtually unlimited unique codes. Stefaan C. De Smedt et al. presented a new approach to increase their encoding capacity while utilizing fluorescence (Figure 3.2(e)). They generated graphical codes by selectively bleaching fluorescent regions with specific patterns [58]. Meanwhile, there are also needs for microtaggants that are able to be ingested, because the incorporation of microtaggants in drugs has attracted attention as an on-dose authentication (ODA) technology for drug authentication. In this context, Stefaan C. De Smedt and co-workers developed similar technologies based on spatial selective photobleaching with FDA approved materials for oral medicines (Figure 3.2(f)) [59]. Our group also developed edible microtaggants that can be utilized for the anti-counterfeiting of drugs as an advanced ODA method (Figure 3.2(d)). In order to contain more information about simple identification in microtaggants, we lithographically encoded Quick response (QR) codes on the microparticle surface. This encoding scheme not only provides a high encoding capacity, but also an error correction function for the damage of the codes. We demonstrated the drug authentication process in the drug formulation with QR-coded microtaggants by using a simple QR code reader application on a smartphone. The information about the drug was successfully retrieved from the QR code on the microtaggant [57].

3.1.2 Physical Unclonable Function (PUF)

Previously examined microtaggant systems could be a solution for preventing counterfeiting crimes due to their high encoding capacity and wide applicability as well as their covert characteristics. In terms of security, however, such technologies also have limitations because their encoding mechanism is predictable, allowing codes to be copied with the same manufacturing system and process used initially to create them. Therefore, more unpredictable encoding mechanisms are required to effectively realize the prevention of counterfeiting.

In this context, physical unclonable function (PUF) gained substantial recognition because it can provide irreplicable features by utilizing intrinsic randomness embodied in a physical structure. Although PUFs have mainly been studied in the field of hardware security, these concepts can be utilized as an encoding scheme by combining with microtaggants [60]. I will briefly introduce representative examples of these PUFs or PUF-like approaches for security applications.

First, R. Pappu et al. presented an optical PUF [61]. They fabricated optical tokens by incorporating glass spheres of 500 μm size in epoxy plates. Then, speckle patterns were obtained by illuminating laser beams on this token as a result of the random scattering of the beam by the glass spheres. These speckle-pattern images were transformed into binary strings (unique identity of the pattern) through hashing for further analysis (Figure 3.3(a)). Since the speckle pattern varies depending on the incidence angle of the laser beam, it should be precisely controlled to obtain reproducible outputs in practical applications.

Next, J. D. R. Buchanan et al. presented a paper PUF concept [62]. They directly utilized the structural randomness of the material itself rather than inducing randomness from outside of the material. The laser scanning of random fiber networks on the surface of the paper resulted in a unique reflection intensity profile, which was different and clearly distinguishable from other papers (Figure 3.3(b)). However, this method lacks applicability to a wide range of products.

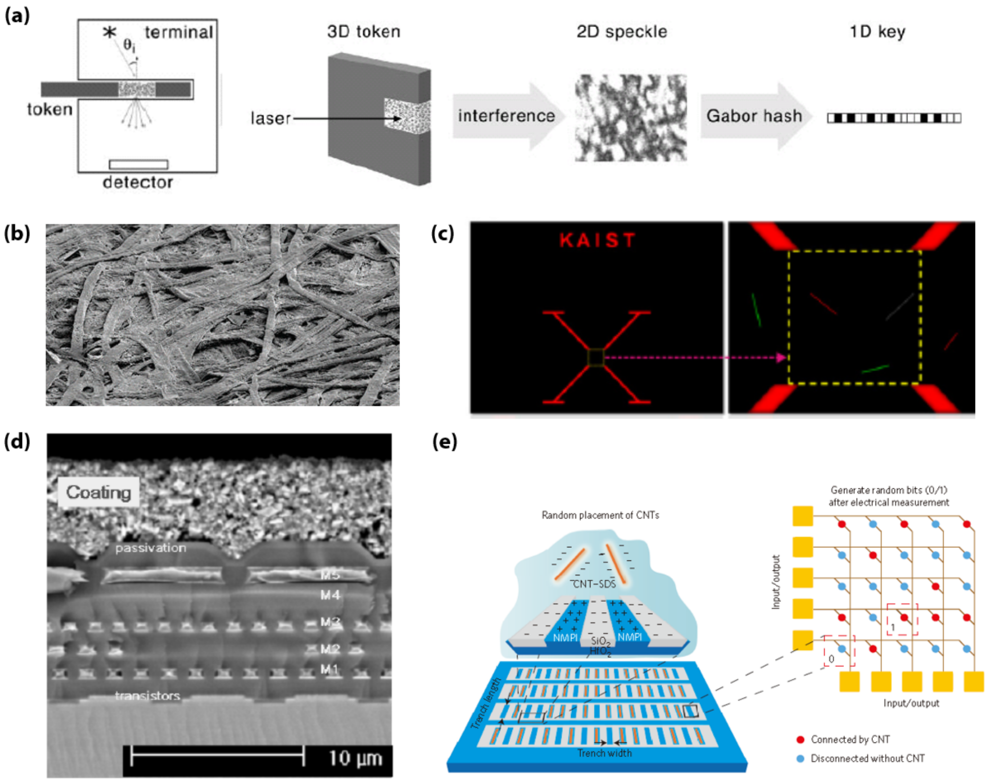

Figure 3.3 Examples of PUF technologies: (a) Optical PUF with random speckle patterns [61]; (b) Paper PUF with random fiber networks [62]; (c) Random distribution of nanowires coated with fluorescent dyes [63]; (d) Coating PUF with random capacitances [64]; (e) Randomized self-assembly of carbon nanotubes to two-dimensional arrays [65].

H. Ihee group presented a PUF-like approach using fluorescence-tagged silver nanowires [63]. They cast the nanowire solution (a mixture of dye coated nanowires with red and green fluorescence and different lengths) on the prepared substrate and utilized their random distribution patterns (Figure 3.3(c)). This approach can provide an unlimited number of unclonable patterns with simple processes by means of the unpredictable fabrication mechanism. However, the short lifespan of fluorescent materials can be a drawback in practical applications.

P. Tuyls et al. developed coating PUFs by fabricating protective coating layers on integrated circuits [64]. The method randomly distributed dielectric particles with different types, shapes and sizes on the aluminophosphate matrix. Then, the array of sensors measured local capacitance values within integrated circuits (Figure 3.3(d)). These kind of PUFs provide a high level of security in integrated circuits, because duplication of these capacitance values is impossible. However, this method is not appropriate to apply to the authentication of general products.

Recently, Z. hu et al. developed a new kind of PUF-like approaches directly applicable in conventional semiconductor processes for the protection of hardwares using carbon nanotubes (CNTs) [65]. This has great advantages for commercial applications. The dimensions of the trench arrays for the CNT were designed to maximize the randomness of the allocation of individual CNT inside the trenches, and the resulting 2D random bit arrays were utilized as unclonable identities (Figure

3.3(e)). This study was the first meaningful demonstration using nanotechnologies in PUF fields, but this was also not appropriate for applications in the authentication of general products, like in the previous paper PUF and coating PUF results.

3.2 Concept of Artificial Fingerprints

As reviewed in the previous section, current microtaggant technologies are unsatisfactory as anti-counterfeiting tags due to their predictable and deterministic encoding mechanisms, despite their versatile applicability to various products. On the contrary, PUF approaches have practical constraints, including noise sensitivity and their limited range of suitable applications, although they guarantee unique and irreproducible codes. Moreover, previously developed PUF-based encoding methods could not provide configurable features, such as code control mechanisms and various decoding strategies. Conclusively, microtaggants and PUF-based methods have not been sufficiently adaptable for anti-counterfeiting strategies at the industry level.

Meanwhile, human fingerprints have been widely used as reliable forensic evidence for criminal investigation. Recently, they have also been used as biometric authentication signatures using scanners or sensor arrays. The unmatched uniqueness of human fingerprints, or epidermal ridges, has been recognized for more than 2000 years, and fingerprint authentication remains the most widely approved method for identifying individuals. Inspired by this valuable function, we mimicked the human fingerprint by patterning random wrinkle patterns on microstructures. Using a PUF-like nondeterministic mechanism, by encoding microparticles with intrinsically random wrinkling, we developed an unclonable and universally-adaptable anti-counterfeiting technology that overcame the discussed limitations of each microtaggant and PUF-based approach. We call this wrinkled microparticle, “the artificial microfingerprint”.

Fingerprints of individual people can be characterized by features called the “minutiae”. The representative types of minutiae are ridge ending (an abrupt ending of the ridges) and ridge bifurcating (a single ridge dividing into two separate ridges). We can also find these minutiae in wrinkled microparticles, because wrinkle patterns consist of a number of ridges (Figure 3.4(a)). Consequently, these patterns can be identified by directly applying conventional fingerprint identification methods. Therefore, for robust product fingerprinting, this new technique earns a distinct advantage due to the already-certified decoding procedures (e.g., error-correction, reconstruction, pattern matching) accumulated over the past 100 years by governments and forensic organizations. Analyzed ridge information of each artificial microfingerprint can be transformed to a binary string, and stored in a server. This data can then be utilized as reference data during the authentication process (Figure 3.4(b)).

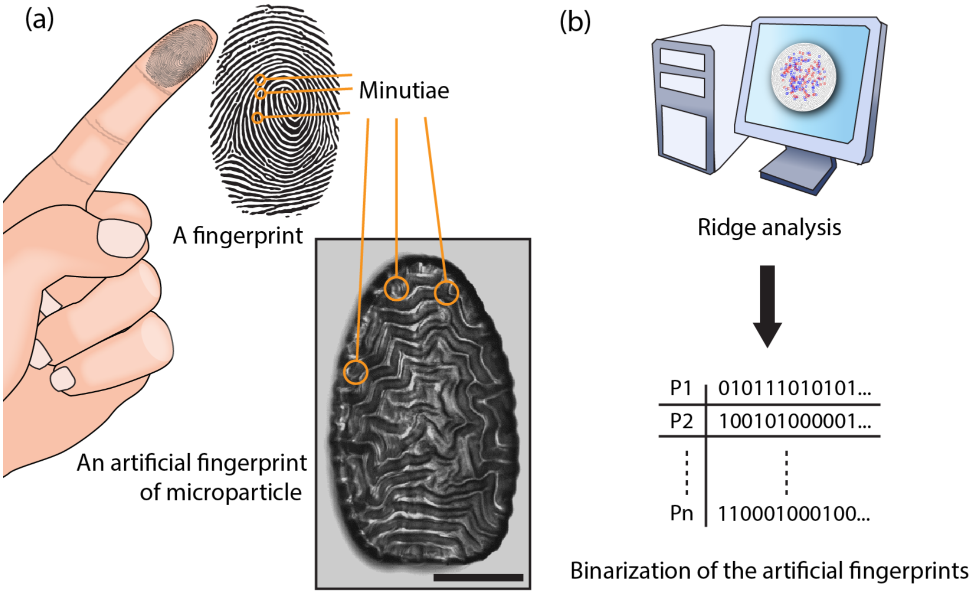

Figure 3.4 Schematic illustration of the authentication system using an artificial fingerprint: (a) Concept of the artificial fingerprint. Wrinkled microparticles possess minutiae points like human fingerprints; (b) Fingerprint analysis process. The ridge distribution of each artificial fingerprint can be stored as a binary string in a server for authentication processes [45].

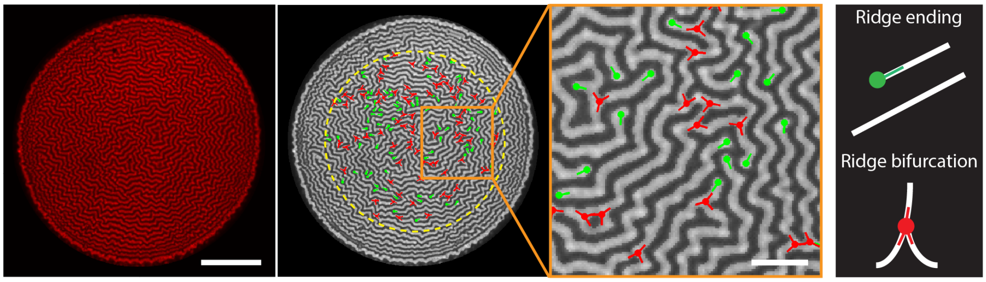

Figure 3.5 Ridge pattern analysis. Ridge ending (green dot) and ridge bifurcation (red dot) points and their angular orientation were extracted from CLSM images of the wrinkled microparticles. 70% of the entire particle surface (yellow dashed line) was utilized for minutiae extraction to avoid inappropriate effects resulting from inhomogeneous strain distribution near the edges (scale bars: 100 and 25 μm, respectively) [45].

Figure 3.5 shows extracted ridge information from an artificial fingerprint. First, the surfaces of wrinkled microparticles were imaged with CLSM. We usually used a 20x lens (NA 0.7) with a 543 nm laser for excitation and a 575 to 600 nm emission filter. Also, we used a 100 Hz or 10 Hz scanning speed for high quality imaging of the wrinkled surfaces. Scanned images were exported to 512 by 512 pixel images with a TIF format. Next, we performed image processing for efficient ridge detection. Then, minutiae information was extracted from the processed images by directly applying conventional fingerprint identification algorithms [66].

In order to maximize the randomness of the ridge patterns, we needed to select appropriate data extraction regions where biaxial in-plane stress dominated wrinkle generation. Therefore, we did not utilized ridges near the edge regions and extracted minutiae from the central area of the surfaces. Moreover, artificial fingerprints were usually synthesized to form a circular disk shape to minimize effect of edges on the wrinkle patterns. When we observed minutiae distribution extracted from several wrinkled microparticles, enough number of minutia points was shown in each microparticle. As a result, we expected the wrinkled microparticles to exhibit significant heterogeneity comparable to human fingerprints.

Figure 3.6 shows the details of the minutiae extraction process. First, we enhanced the ridge pattern in gray scale from the original CLSM images. Next, the particle was moved to the center and was angularly aligned so that the alignment marker faced north. Here, we utilized a sharp indentation as the alignment marker. This kind of structure helps with the robust decoding of the artificial fingerprints with isotropic particle shapes. The varying ridges were then thinned into lines with single pixel widths. This thinning step was required for accurate ridge detection because the minutiae extraction process was sensitive to the width variation of the ridge patterns. Finally, we extracted the positions of the minutia points (ridge endings and ridge bifurcations) and their orientation information.

In summary, wrinkled particles possess PUF-like irreproducible codes that can be decoded using general fingerprint identification processes. Therefore, we expected these wrinkled microparticles could function as biomimetic fingerprints for robust authentication and anti-counterfeiting purposes like biometric systems.

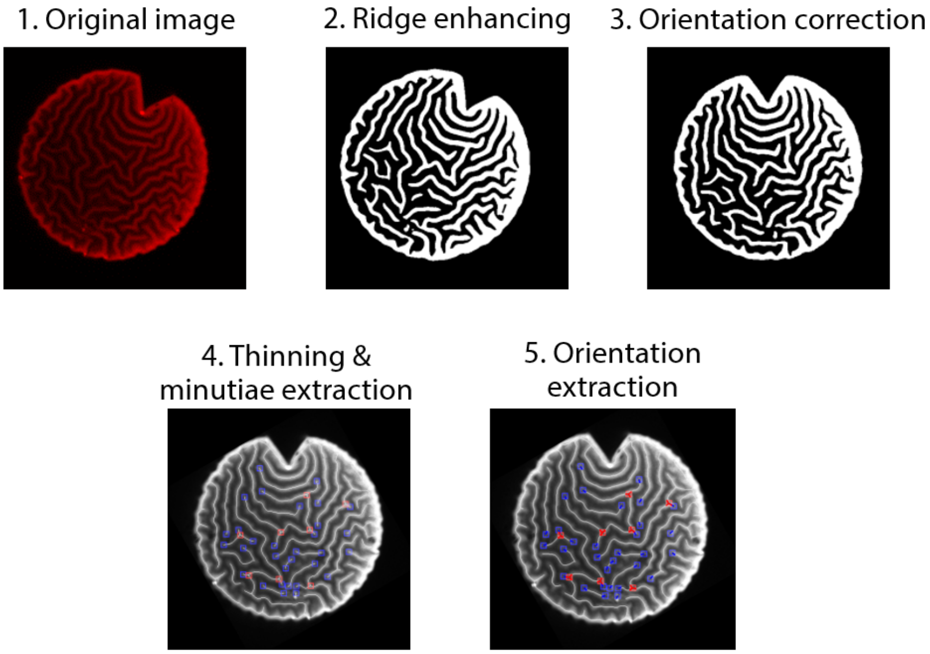

Figure 3.6 Ridge analysis process for artificial microfingerprints.

3.3 Security Level Control

The basic requirement for a smart encoding system is an active mechanism to control codes to tune their capacity or security level. Generally, when we decrease the dimensions of the unit cells of the codes (e.g., the module size in QR codes), data storage capacity increases, while decoding accuracy decreases. In order to implement practical anti-counterfeiting microtaggants, the data capacity and reading accuracy should be flexibly adjusted according to the application purposes (track-and-tracing or forensic authentication) or the decoding conditions (decoder resolution and user experience). However, nondeterministic encoding approaches generally lack this kind of control, resulting in limited applications. Here, our artificial microfingerprints allow the flexible design of the security level by tuning characteristic wavelengths of random wrinkle patterns.

The characteristic wavelength of biomimetic microfingerprints (the average distance between two adjacent ridges) was obtained using the Fast Fourier transform (FFT) analysis on the ImageJ software (Figure 3.7). After importing the original CLSM image, we set the scale with the scale bar information from the image. Then, we performed FFT on the central area of the pattern and found the maximum point with the appropriate noise tolerance. Finally, we were able to obtain distance information. Using this process, we extracted the characteristic wavelengths of the individual artificial microfingperints.

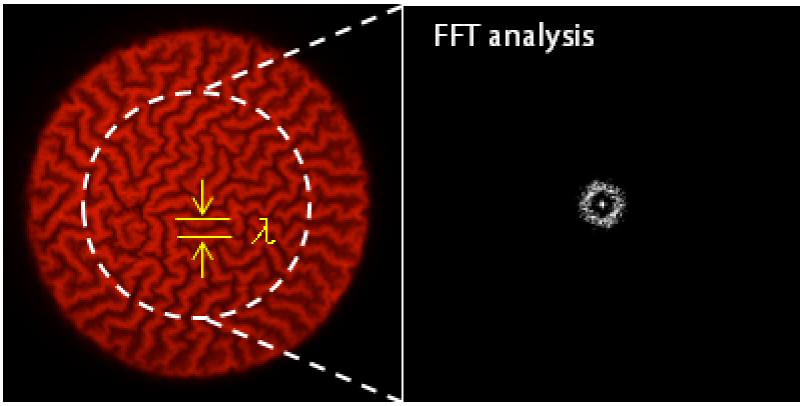

Figure 3.7 Extraction of characteristic wavelength (λ) from the wrinkle pattern. Fast Fourier transform (FFT) analysis was used to measure the wavelength from CLSM images.

The wavelengths of artificial fingerprints can be actively tuned during the fabrication process (Figure 3.8). As explained in Equation (1.1), the wavelength of the wrinkle pattern is proportional to the film thickness t and inversely proportional to the elastic modulus of substrate E_s. We can neglect Poisson's ratios if their effect is smaller than that of the thickness and elastic modulus. Then, the wavelength can be tuned by changing two parameters: t and E_s, which are related to the silica-coating time and the UV light dose for the photopolymerization of substrates, respectively. First, it was reported that the thickness of the silica layer was proportional to the silica-coating reaction time in the Stöber method-based process [67]. Therefore, we verified that the wavelength of wrinkle patterns increased as the coating time increased at the fixed UV light dose. When the coating time was less than 120 minutes, however, wrinkles were not generated. This was because the silica layer formation was incomplete as explained Figure 2.7.

Next, the elastic modulus of substrates is proportional to the cross-linking density of the polymer network. When we illuminated a higher dose of UV light for synthesizing polymeric microparticles, they became denser due to the increased polymerization of monomers, resulting a higher value of elastic modulus. As a result, the characteristic wavelength was decreased as the UV light dose increased. We expected that the presented wavelength range (about 2 to 15 μm) would expand through the further optimization of the parameters and other experimental conditions.

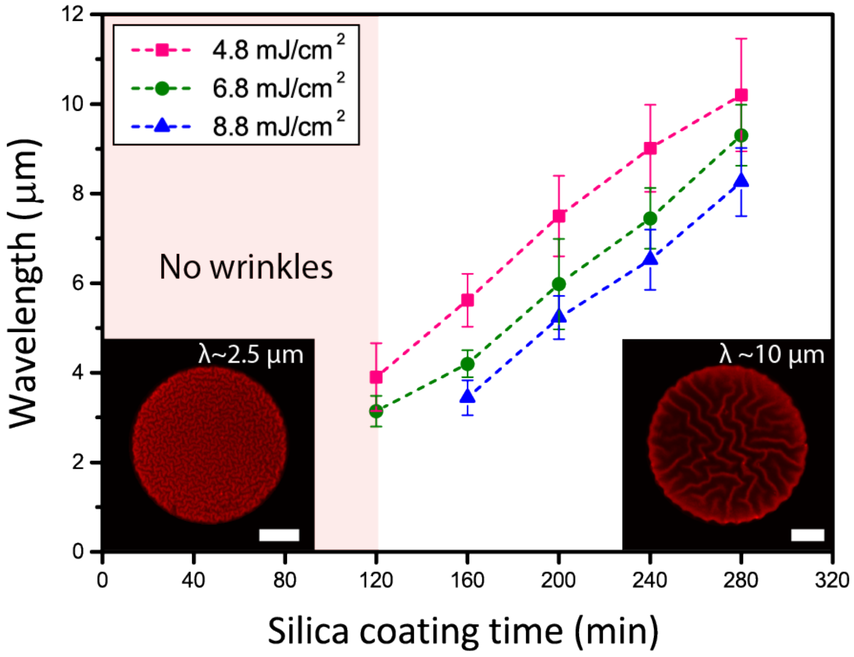

Figure 3.8 Control of the wavelength. The characteristic wavelength of the wrinkle pattern was proportional to silica-coating time and inversely proportional to UV light dose (scale bars: 25 μm). Each data point was obtained from 15 wrinkled microparticles. The error bars represent the standard deviation of the wavelength [45].

The configurable property of the wavelength can be directly applied to the design of security levels on artificial microfingerprints. When we plotted the distribution of minutia densities (the number of total ridge endings and bifurcations per unit area on each wrinkled microparticle) based on the wavelength using microparticles databased in Figure 3.8., the density was inversely proportional to the wavelength (Figure 3.9). Since the security level of the artificial fingerprint is proportional to the minutia density, we can classify the artificial fingerprints according to their characteristic wavelength. For example, we can divide the fabricated artificial fingerprints to three different levels, H, M, and L. Although the representative images of the artificial fingerprints in Figure 3.9 clearly show different security levels or code complexities, it seems to be ambiguous to define the boundary of the security level in the graph, because the dispersion of the density was large at some wavelengths. However, we need to provide more distinct classifications of the security levels on artificial fingerprints for practical applications. We expected the overlap of the density distribution would be reduced by confining the wavelength of artificial microfngerprints to specific values with enough distance, like microparticles in the representative images. Then the security level could be classified more clearly.

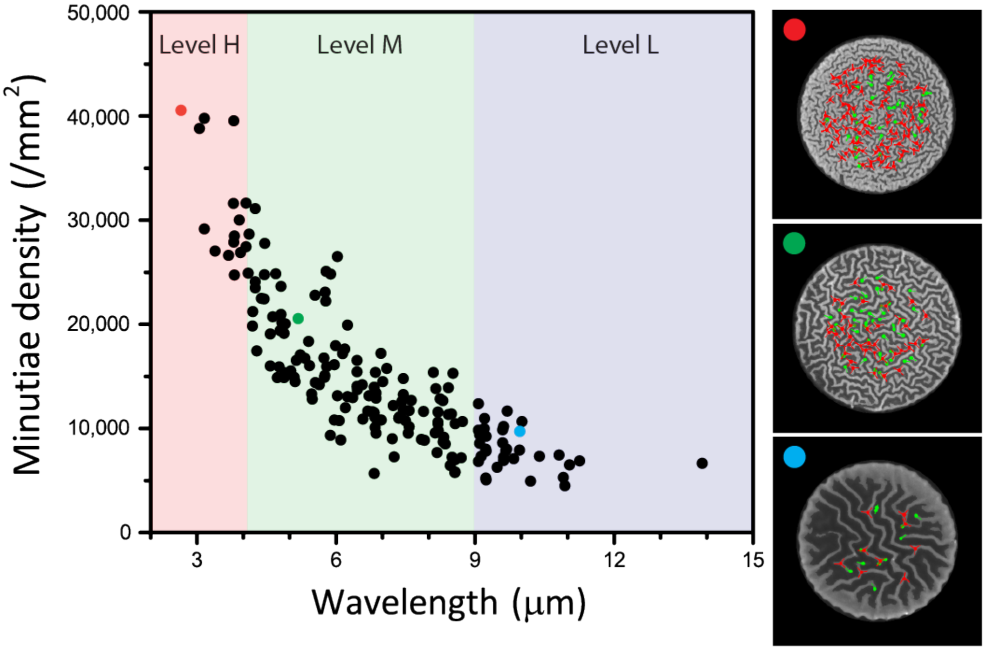

Figure 3.9 Control of the security level. The security level, or minutiae density, can be classified by the wavelength of the wrinkle pattern. The right images show representative images of the artificial fingerprint in each security level (H, M, and L) [45].

In addition to the security level, the code capacity of the artificial fingerprints was configurable by changing the particle size. We calculated the producible numbers of artificial fingerprints. First, we assumed that the particle diameter was 100 μm and the minimum characteristic wavelength was 2.5 μm. Then, we divided the 100 μm circle using orthogonal grids with a spacing of 2.5 μm. As we considered only the inner 70% of the entire circle area, approximately 600 intersections corresponded to the possible number of minutia points. Also, we assumed that there was one type of producible minutia (e.g., only ridge ending), and the maximum number of producible minutia was approximately 130, based on the repetitive experimental results. Consequently, we were able to calculate the code capacity as ${}_{600}C_{130} + {}_{600}C_{129} + {}_{600}C_{128}\ldots \approx 10^{135}$, which is virtually infinite. This estimated code capacity is the maximum value of the circular particle with a diameter of 100 μm, and can be changed if we confine the wavelengths of fabricated artificial fingerprints to specific values.

In this context, we were able to tune the code capacity by changing the size of the artificial fingerprints (Figure 3.10). The code capacity increased with size at fixed wavelengths, due to the increased number of minutia points in the artificial fingerprints. In addition, we can further expand the code capacity by utilizing other minutia types (like bifurcation and island) and their unique spatial distributions.

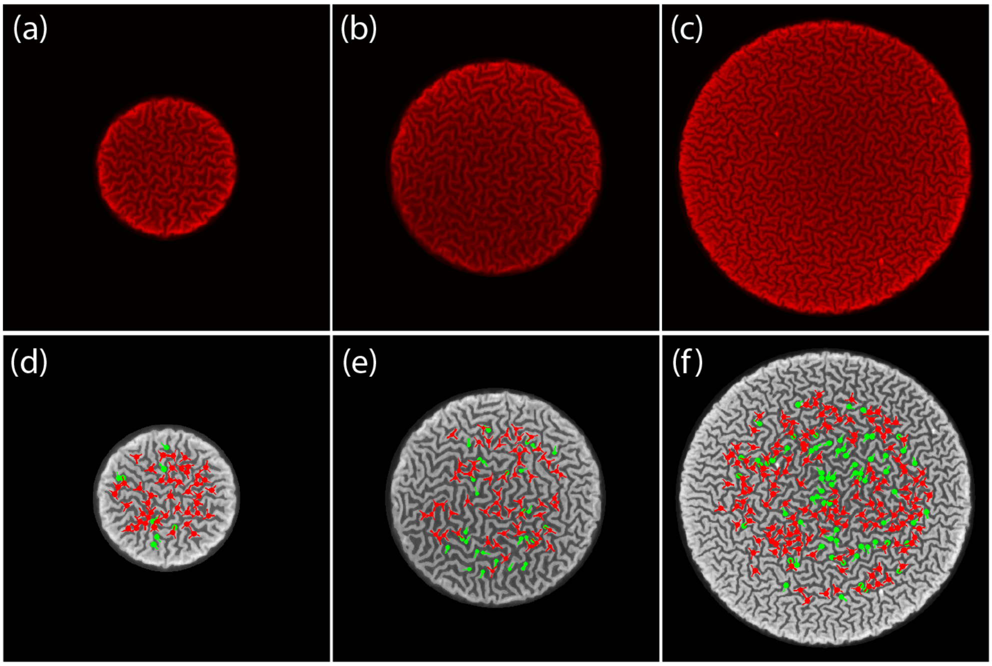

Figure 3.10 Control of the code capacity based on the particle size: (a-c) CLSM images of wrinkled microparticle surfaces. The particle size is 53, 80, and 113 μm, respectively while the wavelength is approximately fixed to 4 μm: (d-f) Extracted minutia distribution. Green dots and red dots represent ridge endings and ridge bifurcations, respectively. The total number of minutia was 53, 90, and 212, respectively [45].

We verified that the security level and the code capacity of the artificial fingerprints can be flexibly designed by tuning their wavelength and size. In addition, our artificial fingerprints can provide code categorization according to the shape of artificial fingerprints (Figure 3.11). The wrinkled microparticles can be fabricated with any shapes using the OFML system, unlike human fingerprints. We c generated artificial fingerprints with alphabet letters as well as basic geometries. Although these particle shapes possess reduced code randomness compared to the circular shape, we can provide additional information using these shape codes in addition to random topographical codes, at the expense of the security level. This capability enables the creation of numerous classes of artificial fingerprints and the categorical labeling of numerous products on user demand.

Overall, we presented randomized, but configurable authentication microtaggants by implementing wrinkle patterns on microparticle substrates. This biomimetic microfingerprint platform provides not only unclonable codes with a nondeterministic encoding mechanism, but easy manipulation of the security level and the taggant class, that were infeasible in most previously developed PUF-based anti-counterfeiting methods.

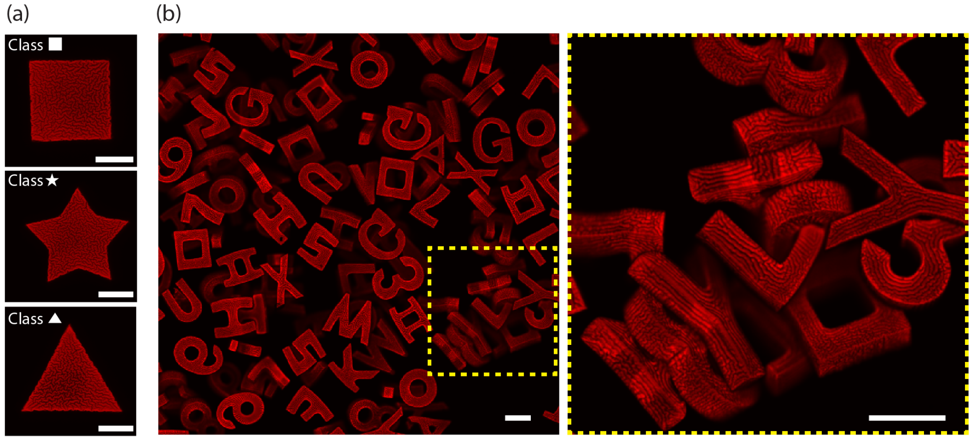

Figure 3.11 Classification of the artificial fingerprint by its shape: (a) Simple shapes. Square, star, and triangle shape of the particle (scale bars: 50 μm); (b) Various shapes. Wrinkled microparticles can also have shapes like letters or numbers. (scale bars: 100 μm) [45].

3.4 Individuality Analysis

Although we recognize the presented wrinkling-based encoding produces unclonable codes, we still need to verify the uniqueness of the fabricated artificial fingerprints. In this section, I present the analysis results performed to study the individuality of the artificial microfingerprints.

First, the uniqueness of artificial fingerprints was evaluated by observing the cross-correlation values between them. For a large scale analysis, we fabricated several thousand polymeric microparticles with the alignment key and coated them with silica in a single batch process. We then dried the silica-coated microparticles in several wells of a 96-well plate to fabricate artificial microfingerprints. We controlled the number of microparticles in a single well in order to minimize overlapping. After discarding damaged, contaminated, or un-wrinkled microparticles, we imaged the individual artificial fingerprints and obtained 200 fingerprint patterns using CLSM (Figure 3.12) and obtained the first scanned image set. Each artificial fingerprint was also imaged a second time after a routine task to obtain the second scanned image set.

From the obtained images, we extracted the locations of ridge endings and ridge bifurcations. This spatial distribution information of each image was transformed to a minutia matrix with the same size as the original image (512 by 512). The positions where minutia points existed were stored as 1 and the others as 0. However, if we set ridge ending points or bifurcation points to one pixel, a small

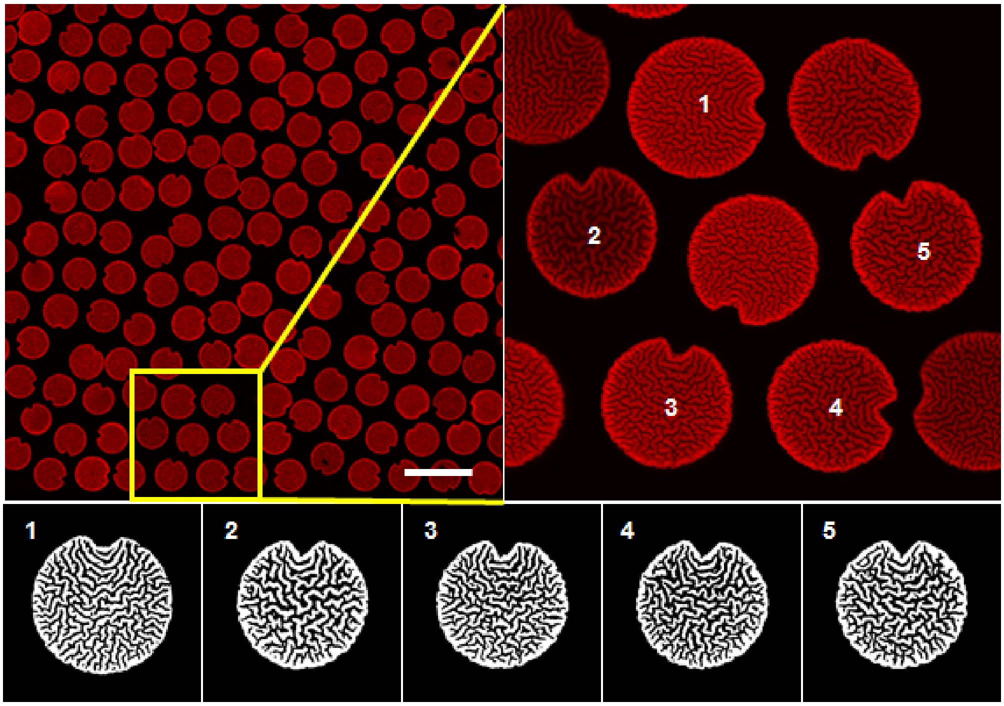

Figure 3.12 CLSM imaging of wrinkled microparticles for large scale data analysis. Sharp indentations shown in the magnified image were utilized for angular alignment keys (scale bars: 200 μm) [45].

rotation or distortion of the pattern images can result in different cross-correlation values. In order to minimize these kind of pixel errors in cross-correlation analysis, we provided reasonable tolerance by using a two-dimensional Gaussian distribution from the minutia-located coordinates within a given pixel range. After this filtering, we calculated the cross-correlation values between two image sets by performing sliding inner-product of every combination of two minutia matrices (Figure 3.13). The intra-correlation (correlation between different images from the same artificial fingerprint) showed higher values than the inter-correlation (correlation between different artificial fingerprints), and they were clearly distinguishable. This revealed that each artificial fingerprint possessed a distinct wrinkle minutia pattern.

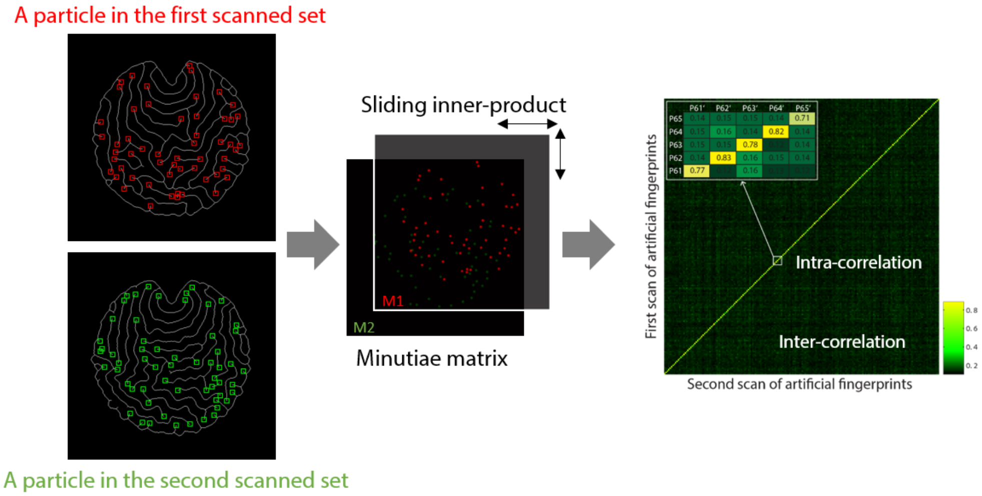

Figure 3.13 Evaluation of performances of the artificial microfingerprint for the authentication system. The cross-correlation values were calculated using extracted minutia distribution information from 200 artificial fingerprints [45], [68].

Next, we investigated the level of individuality of artificial fingerprints using image-hashing-based correlation analysis, which is commonly adapted in human fingerprint analysis. For this purpose, we converted minutia information to a binary string and obtained the corresponding hash key by modifying the previously developed minutia hashing algorithm [69]. Figure 3.14(a) shows a schematic illustration of the analysis process. For each ridge point, we extracted the distance from the particle center to the point d, the radial angle of the point θ, and the radian angle of the ridge orientation α. For ridge bifurcations, we defined α as the radian angle of the vector dividing the smallest angle among three angles in half. Then, for each minutia point, these values were transformed into binary numbers and joined to a new binary number. This joined binary number was again converted into a decimal number as an address where "1" is stored at its corresponding address in a large binary string. Finally, this large binary string was converted into a hash key, which is a unique ID of an artificial fingerprint. In order to measure the individuality of artificial fingerprints, we calculated correlations using the 200 artificial fingerprints databased in Figure 3.13 and their hash keys (Figure 3.14(b)). The inter-class distribution (correlations between different artificial fingerprints) and the intra-class distribution (correlations between different hash keys from the same artificial fingerprint) were well separated like previous cross-correlation analyses, which verified the uniqueness of the artificial fingerprints.

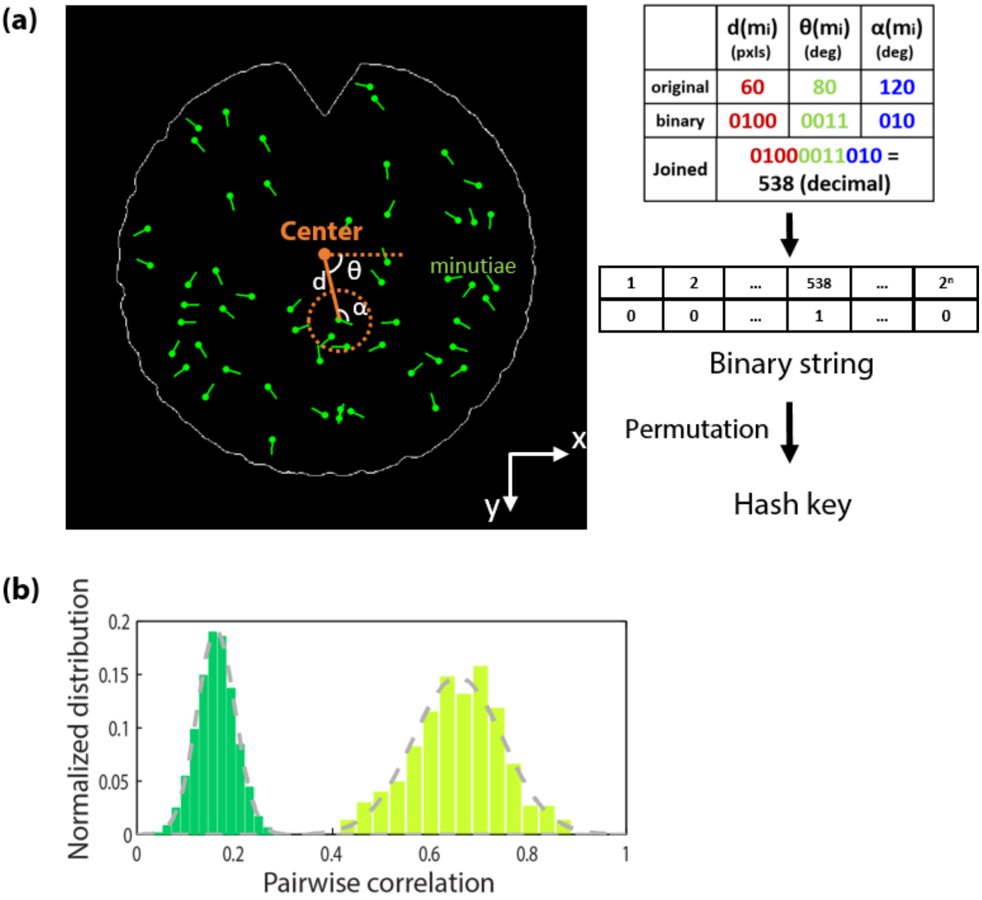

Figure 3.14 Individuality analysis of artificial microfingerprints using a hashing method: (a) Generation of hash keys from minutia information [68]; (b) Distribution of hashing-based correlation values obtained from hash keys of the artificial fingerprints. The mean correlation values and the standard deviation of the inter-class distribution (green) were 0.16 and 0.039, respectively. The mean correlation values and the standard deviation of the intra-class distribution (light green) were 0.66 and 0.092, respectively [45].

Finally, the level of individuality of artificial fingerprints was investigated by comparing them with that of human fingerprints. For this purpose, we analyzed the degree of randomness of minutiae distribution from both artificial fingerprints and human fingerprints. Since we could not directly utilize human fingerprints due to privacy issues, we purchased a license for an official fingerprint generation software, SFinGe, and generated synthetic human fingerprints for the analysis [70]-[73]. The representative images of synthetic human fingerprints and artificial fingerprints are shown in Figure 3.15(a) and (b), respectively. The minutia extraction area (orange circled region) was selected to satisfy the same ratio of the characteristic wavelength (average of all samples) to the data collection area diameter in both synthetic human fingerprints and artificial fingerprints groups. Also, in order to control the total minutia number in both groups to similar values, we obtained minutia data from 1,000 synthetic fingerprints and 300 artificial fingerprints, because the number of minutia in artificial fingerprints were 3.5 times higher than that of synthetic fingerprints on average.

When we compared the spatial distribution of minutia points, both synthetic human fingerprints and artificial fingerprints showed uniform distribution in the code extraction area (Figure 3.16). This revealed that minutia points were randomly located in both fingerprints and they possessed similar individuality in terms of spatial distribution.

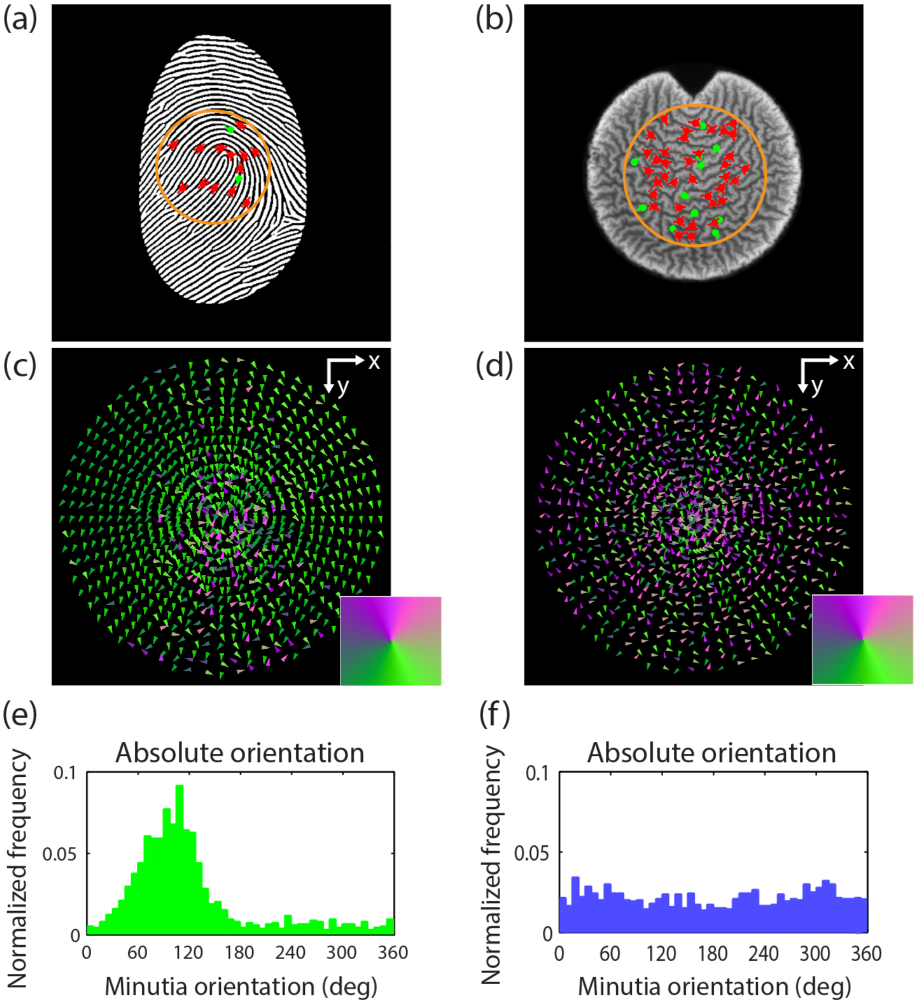

Figure 3.15 Comparison of individuality between artificial fingerprints and human fingerprints: (a) Representative image of a synthetic human fingerprint; (b) Representative image of an artificial fingerprint; (c) Vector field display of average orientations of ridge endings from synthetic fingerprints. Each vector presents the averaged orientation data in the corresponding bin. The color map at the bottom-right corner defines the orientation coordinate; (d) Vector field display of average orientation of ridge endings from artificial fingerprints; (e) Normalized distribution of vector orientations in (c); (f) Normalized distribution of vector orientations in (d) [45].

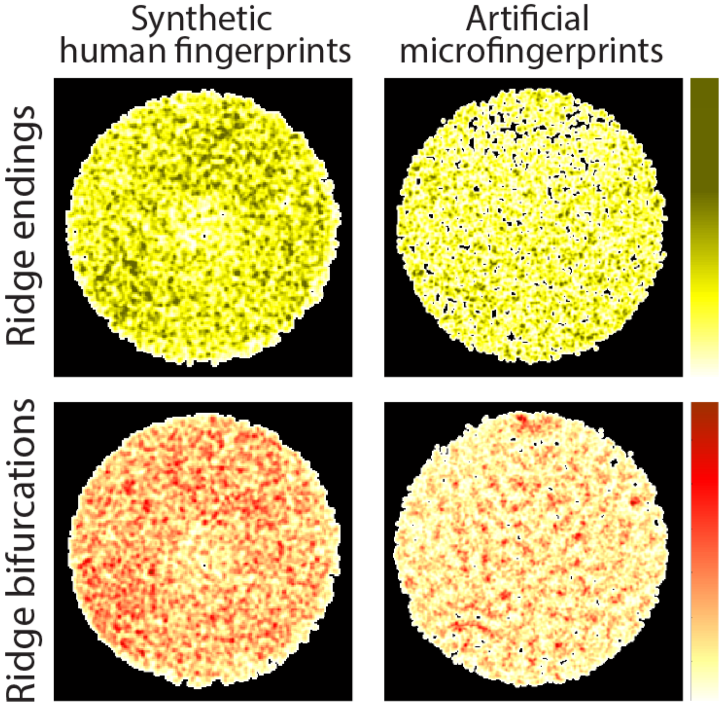

Figure 3.16 Spatial distribution of minutia within the collection area for both synthetic fingerprints and artificial fingerprints. The color bars indicate the relative density of ridge points. Darker colors represent higher densities [45].

On the contrary, when we compared the angular orientation of ridge ending points, both synthetic human fingerprints and artificial fingerprints showed different distributions. When the averaged vector fields of the ridge ending orientation were plotted, the synthetic fingerprints showed biased distribution (Figure 3.15(c), (e)). This may have resulted from the fact that human fingerprints are limited to a few common categories such as loops, whorls, and arches. Therefore, the orientation of ridge endings were similar within each category. On the other hand, the artificial fingerprints showed unbiased and even orientation distribution (Figure 3.15(d), (f)). In addition, we plotted the Lorenz curves of minutia orientations for both fingerprints and extracted Gini coefficients to investigate the statistical dispersion. Then, the artificial fingerprints showed a smaller Gini coefficient, which verified a more uniform and randomized distribution of the ridge orientation in artificial fingerprints.

In summary, based on the performed individuality analyses, we can conclude that the biomimetic microfingerprints possess unique codes, and contain a more randomized distribution of the minutia orientation than the synthetic fingerprints, thus providing a higher level of individuality, even compared to human fingerprints

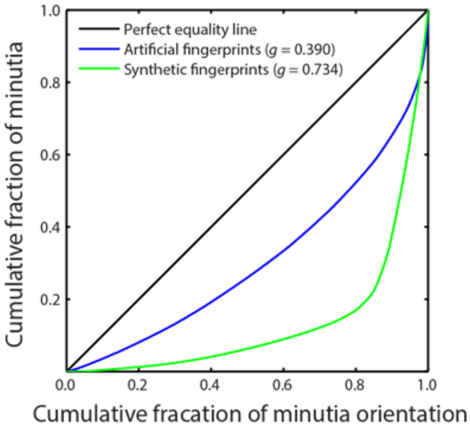

Figure 3.17 Lorenz curves of the histograms in Figure 3. 15. The Gini-area values were 0.390 for artificial fingerprints and 0.734 for synthetic fingerprints [45].

3.5 Demonstration

In this section, the applications of the biomimetic fingerprints will be demonstrated as microtaggants for anti-counterfeiting purposes. First, we found appropriate coating materials for attaching the artificial fingerprints on the surface of products. After generating wrinkles on microparticles, we dispensed several candidate materials on wrinkled microaprticles and observed their surfaces in order to check whether the wrinkle patterns could be imaged or not (Figure 3.18). After dispensing the ETPTA and norland optical adhesive (NOA) on the surface of microparticles, they were illuminated with a UV light. For the super glue and liquid glue, we waited until they were completely solidified. For PDMS, we prepared PDMS bases mixed with a curing agent and heated PDMS coated microparticles inside an oven heated to 80 ^{o}C for 20 minutes. As shown in Figure 3.18, some constituents of the super glue severely disturbed the imaging of the patterns as well as the ETPTA and NOA fabricated layers covering certain pattern regions. Also, wrinkle patterns were not observable after coating with the liquid glue. It seemed that the liquid glue percolated through the cracks on the silica surface and modified the surface pattern. However, the PDMS-coated wrinkled microparticles showed clear wrinkle patterns like the untreated wrinkled microparticles had. Therefore, we decided to utilize PDMS coatings as the protection layer of the artificial fingerprints on the product surfaces.

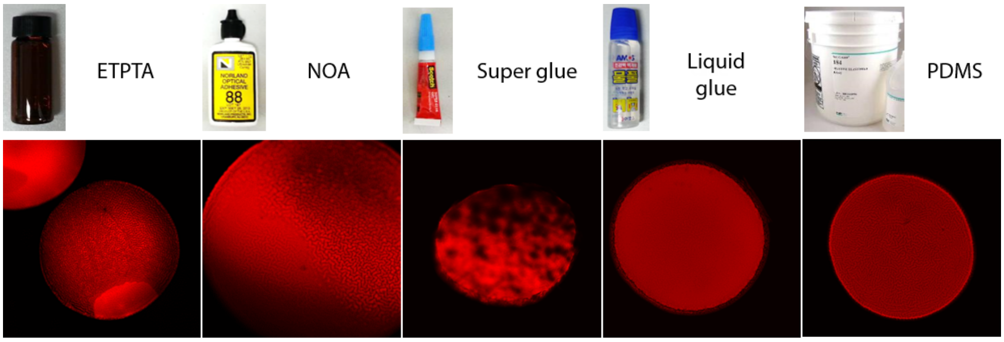

Figure 3.18 Candidate materials for protection layer of artificial fingerprints. After coating the artificial fingerprint surface with each material, the surface was imaged using CLSM.

Generally, the security level of codes correlated with the decoding accuracy or required decoder resolutions. In the previous sections, we verified that the security level of our artificial microfingerprints could be tuned by changing the characteristic wavelengths of the wrinkle patterns at the fixed particle size. In order to practically utilize these configurable microtaggants, we also need to provide appropriate decoding strategies according to the code complexity, determined by application properties or user demands. For example, high-performance devices like a confocal laser scanning microscope are available for lab-oriented forensic authentication, whereas field-oriented authentications like track-and-tracing require decoders to be user-friendly and portable.

To validate the universal applicability of the artificial fingerprinting approach, we attached the biomimetic fingerprints to common products and tested out various

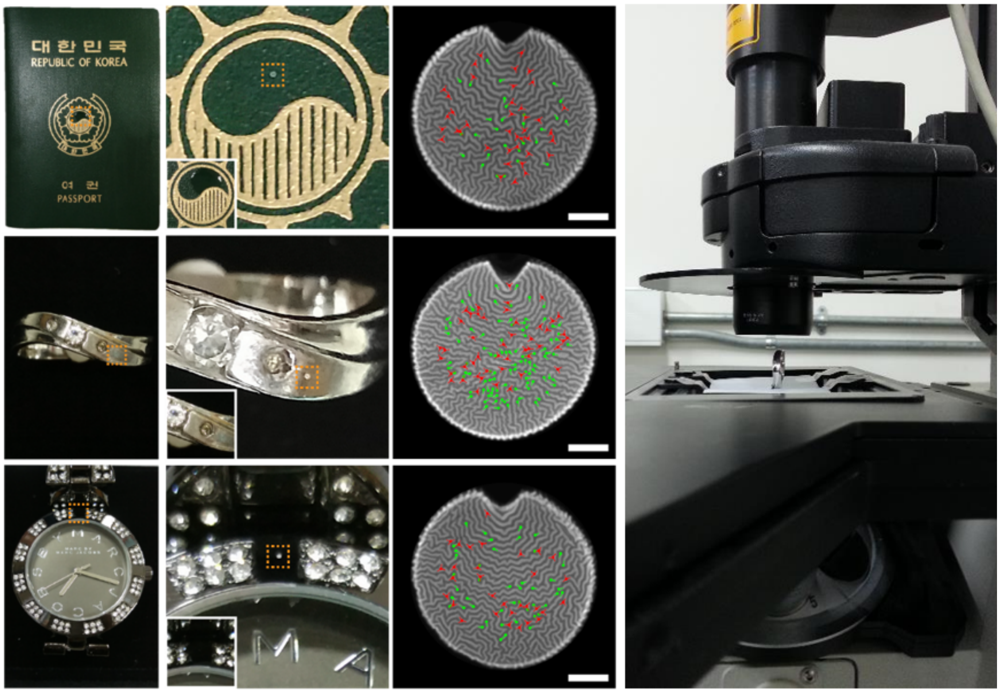

Figure 3.19 Demonstration of artificial fingerprints as anti-counterfeiting microtaggants for commercial products. Right image shows authentication of the taggants attached on the product surface using CLSM (scale bars: 50 μm) [45].

optical decoding methods. First, we fabricated the artificial fingerprints with a high level of security by generating wrinkle patterns with wavelengths of a few microns. After locating these artificial fingerprints on appropriate locations of the product surfaces, we dispensed one drop of PDMS and heated the taggant-attached products in an oven (Figure 3.19). Detection of the artificial fingerprints was not easy with the naked eye after the formation of the PDMS protection layer. Because the pattern wavelength was only a few microns, topographical codes in the attached artificial fingerprints were detectable only with CLSM. We successfully scanned the artificial fingerprints even on curved surfaces by appropriately placing the products on CLSM. Consequently, we verified that the presented biomimetic microtaggants can be applied for powerful anti-counterfeiting purposes including forensic science.

On the other hand, the artificial fingerprints with large wavelength patterns (up to 20 μm) were readable using a commercially available portable microscope (200x) that was attached to a smartphone (iPhone 6). Although we did not develop the minutia extraction algorithms for bright-field images here, these artificial fingerprints with lower security levels suggest the possibility of a field authentication (e.g., track-and-tracing) requiring optical decoders with low resolution. Overall, our designable artificial fingerprinting would expand the applicability of PUF-based taggants to a broad-range of optical authentication methods.

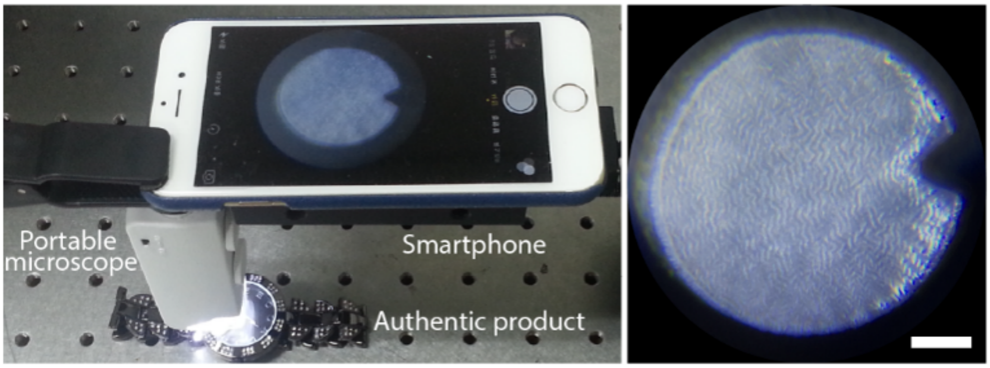

Figure 3.20 Decoding of artificial fingerprints using portable microscope that can be attached on a smartphone (200x) (scale bars: 100 μm) [45].

For practical applications, it is imperative that the artificial fingerprints be stable in various environments. We performed several tests in order to evaluate the durability of our biomimetic microfingerprints.

First, we examined whether the artificial fingerprints were able to retain their wrinkle patterns when re-immersed in solvent. Figure 3.21 shows that the wrinkle pattern was preserved after the re-swelling process in ethanol, although the particle size and the characteristic wavelength of the wrinkle pattern slightly increased due to the swelling of the polymer substrate. As a result, patterns encrypted on the silica-layer could not undergo a reverse process once the wrinkle patterns appeared on the microparticle. In this regard, protecting microparticles from exposure to air before completing the silica-coating process is important to achieve configurable encoding.

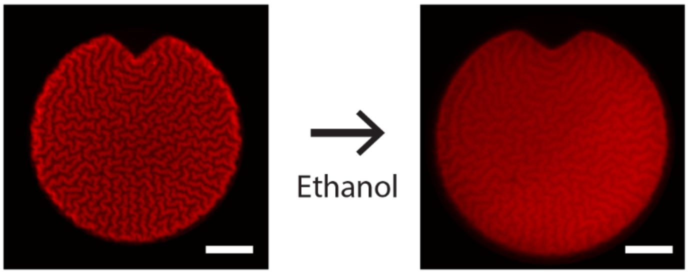

Figure 3.21 CLSM image after swelling wrinkled microparticles in ethanol (scale bars: 25 μm).

To clarify further, we repeatedly performed shrinking and swelling processes and calculated the cross-correlation values using the images of five artificial fingerprints taken at each cycle. As shown in Figure 3.22(b), the artificial microfingerprint seemed to preserve its code even after the re-swelling had subsided. We then extracted minutia information from the obtained images of different artificial microfingerprints (P1 ~ 5) in their dried state, and calculated the cross-correlation values between the images. As a result, high intra-correlation values (for example, P1 – P1, diagonal steps of the heat map) were clearly distinguishable with relatively low inter-correlation values (for example, P1 – P2) as shown in the Figure 3.22(a). This revealed that each artificial fingerprint maintained its unique code from the repeated swelling and shrinking. Overall, we could conclude that our artificial microfingerprint-based authentication system was robust enough to prevent a counterfeit attack, even under the swelling conditions.

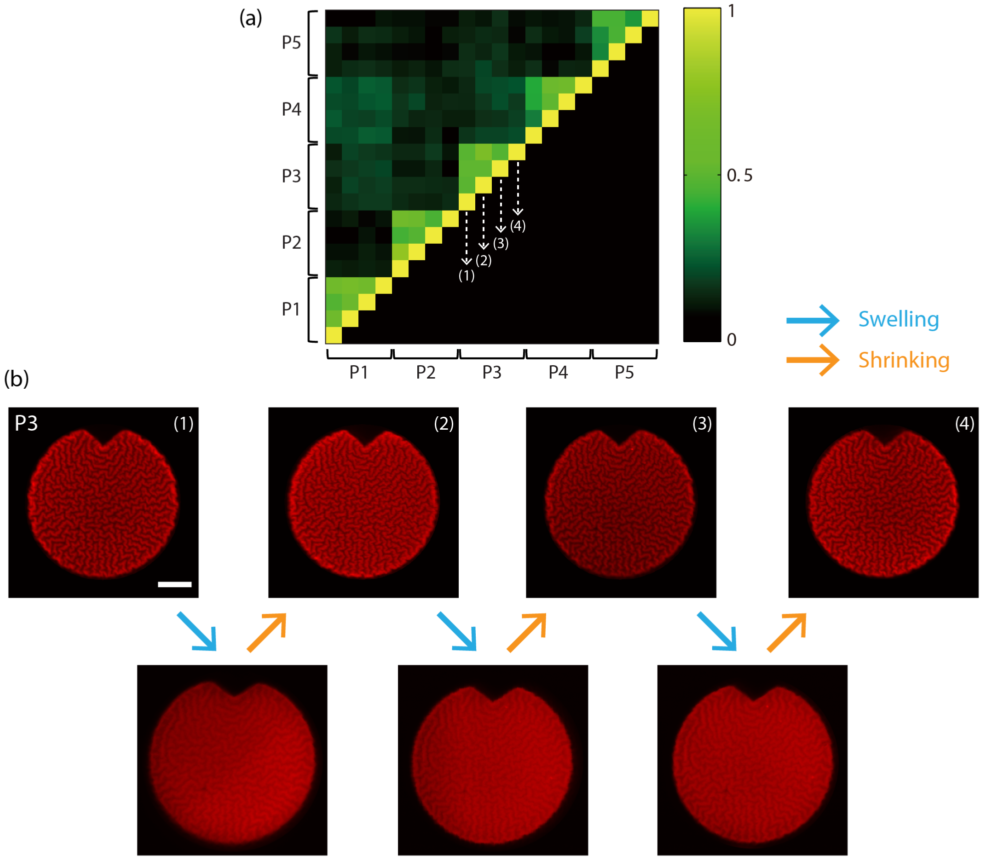

Figure 3.22 Stability test in repetitive swelling and shrinking processes: (a) Heat map of normalized cross-correlation values obtained from five different dried artificial fingerprints; (b) CLSM images of the representative artificial microfingerprint in each swelling and shrinking step (scale bars: 25 μm) [45].

Second, the stability of the artificial fingerprints was tested under a high temperature condition because artificial microfingerprints can be damaged and lose their unique wrinkle codes from excessive heat. Although the silica shell of the artificial fingerprint has strong thermal stability because the melting point of silica is higher than 1,500 °C, the core polymeric substrate can be damaged under harsh conditions. In order to verify the thermal stability of our artificial microfingerprint, we heated them on a 200 °C hot plate. After beginning to heat, we imaged several artificial fingerprints (P1 ~ 5) every 6 hours for a day. We then extracted minutia information from the obtained images (0, 6, 12, and 24 hour heating) for these artificial fingerprints, and calculated the cross-correlation values between images. As shown in Figure 3.23(b), damage of the particle was not observed during the 24 hour heating period and the minutia were successfully extracted. Furthermore, we found higher intra-correlation values (for example, P1 – P1, diagonal steps of the heat map) compared to inter-correlation values (for example, P1 – P2) as shown in the heat map (Figure 3.23(a)). This verified that each minutia pattern encoded in the artificial fingerprints were preserved by the heating process. However, relatively low correlation values were observed in the first column of each intra-correlation region. The shrinkage of the polymer substrates after heating resulted in lower correlations between the unheated and the heated artificial microfingerprints. However, these kind of decoding errors can be avoided by preheating the artificial fingerprints for a few hours before the initial scanning of the codes, because the degree of the particle shrinkage was insignificant after a few hours of heating. Overall, we can conclude that our artificial microfingerprint-based authentication system is robust under high temperature conditions.

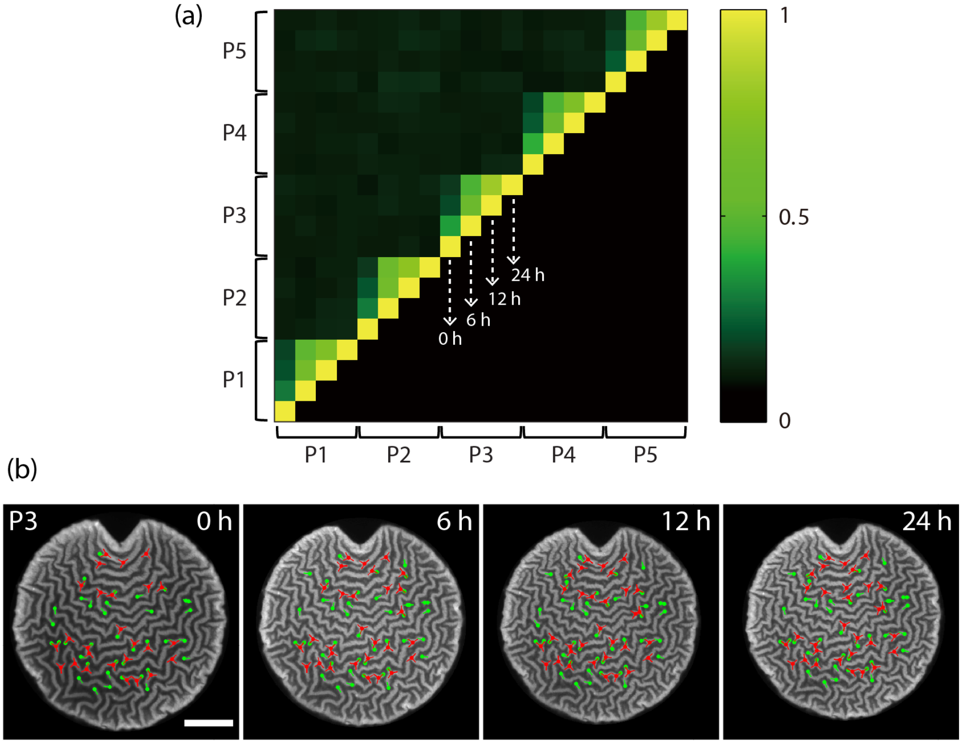

Figure 3.23 Stability test under thermal damage: a) Heat map of normalized cross-correlation values obtained from heated five different artificial fingerprints. Artificial fingerprints were heated on a 200 °C hot plate; (b) CLSM images of the representative artificial microfingerprint after different heating periods (scale bars: 25 μm) [45].

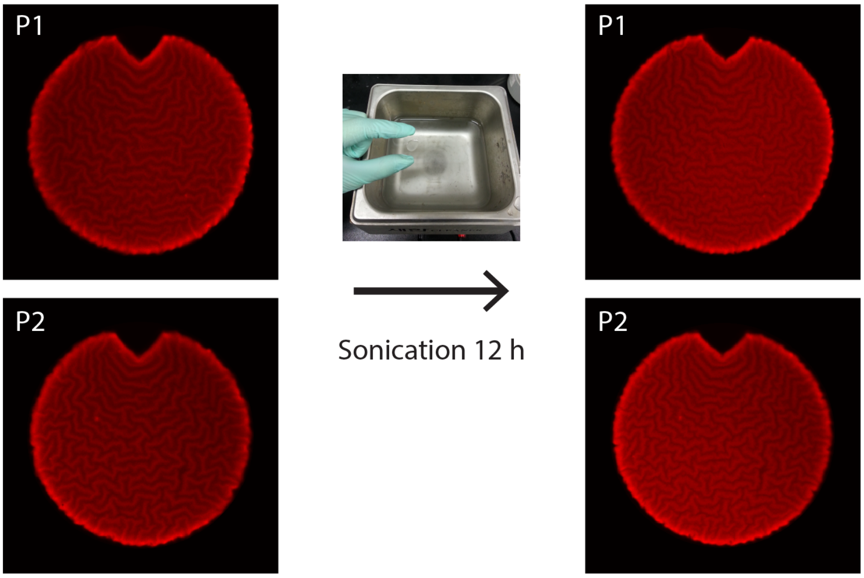

Figure 3.24 Stability test under physical damage using sonication. CLSM images of artificial fingerprints before and after 12 hours of sonication show no evidence of physical damage [45].

Finally, the stability under mechanical stress was tested using sonication (Figure 3.24). For this purpose, artificial microfingerprints on a cover glass were coated with PDMS and then were sonicated in a sonicator bath. Damages to particles and wrinkle patterns were not detected during the sonication process for a period of 12 hours.

In summary, wrinkled microparticles were presented as artificial fingerprints that were the first taggants utilizing human fingerprint technology. We identified that human fingerprint-like features, the minutiae, were abundant in randomized wrinkle patterns. These biomimetic fingerprints possessed considerable individuality and physical unclonability, which forbade the reproduction of existing taggants even for the original manufacturer. Furthermore, we developed unique fingerprint designing mechanisms that allowed the security level and code capacity of these random codes to be controlled. Therefore, our approach provided mature code controlling mechanisms to match the technical specifications of various products and their corresponding read-out architectures. These low cost taggants also guaranteed a long lifespan and environmental inertness. Therefore, this new type of taggant fulfills the most demanded requirements for an industry-suitable, unclonable authentication strategy. We believe the artificial fingerprint would find applications in various fields, including track-and-trace and forensic authentication. Furthermore, this highly secure and flexible authentication strategy can become a definitive solution to the enormous counterfeit market and have positive impacts on the field of authentication and anti-counterfeiting.

However, it is still possible that the topographical codes of the artificial fingerprints can be copied by molding their surface structures using soft lithography methods or printing using a 3D printer, despite the non-deterministic encoding scheme. In order to prevent the duplication of the taggant itself, the wrinkle patterned surface can be coated again with other materials, such as ceramics or metals using thermal spraying or e-beam deposition. The post-coating process after the registration of the artificial fingerprint can prevent the replication of the unique topographical code by modifying the original topography, while users can decode the correct wrinkle pattern at the original polymer and silica interface through fluorescent dye incorporated into the polymer substrate on the CLSM. In addition, several wrinkle patterns fabricated from different wavelengths (from submicron to micron) can be generated in one microparticle in order to impede duplication of the multiple ridge patterns in various length scales using molding or printing methods within one material system.

Chapter 4

Patterning Controlled Wrinkles

In this chapter, several control methods for random wrinkles are presented. First, the tuning of the degree of randomness will be demonstrated based on the particle shapes or ratio of the particle size to the pattern wavelength. Also, the partial alignment of the ridge orientation will be demonstrated by changing the internal structure of the particle. Second, an elaborate wrinkle control technique allowing precise guiding of individual ridges to intended directions will be introduced.

4.1 Rough Control Methods

In this section, some low-level wrinkle control mechanisms in the particle-based substrates are briefly discussed. The shape of the particle, or the geometry of the particle edge, has an influence on the ridge pattern near that edge region. Consequently, the area governed by equibiaxial stress is changed according to the edge geometry. Using these fundamentals, we could control the pattern randomness on microparticles (Figure 4.1). At the similar surface area and characteristic wavelength conditions, the randomness was at its maximum in the circular shape. In rectangular shapes, the ridges tended to converge at the corners and ran parallel at the sides, which decreased the pattern randomness.

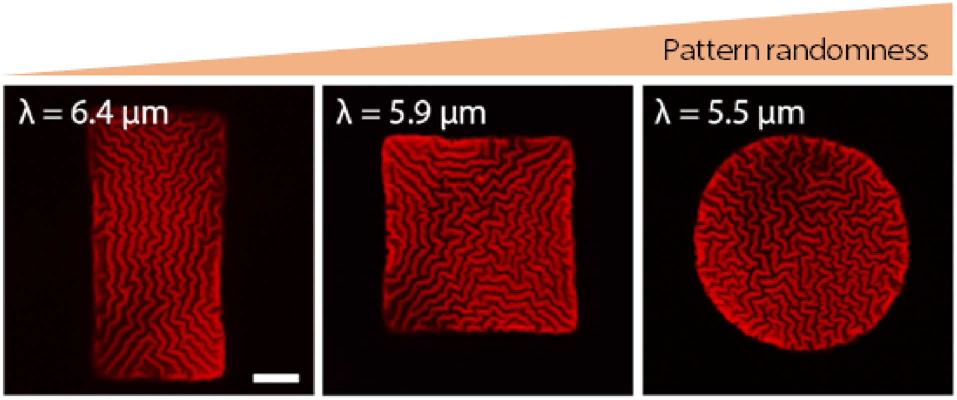

Figure 4.1 Control of orientation randomness by changing the particle shape while maintaining similar surface area and characteristic wavelength at each microparticle (scale bar: 25 μm) [74].

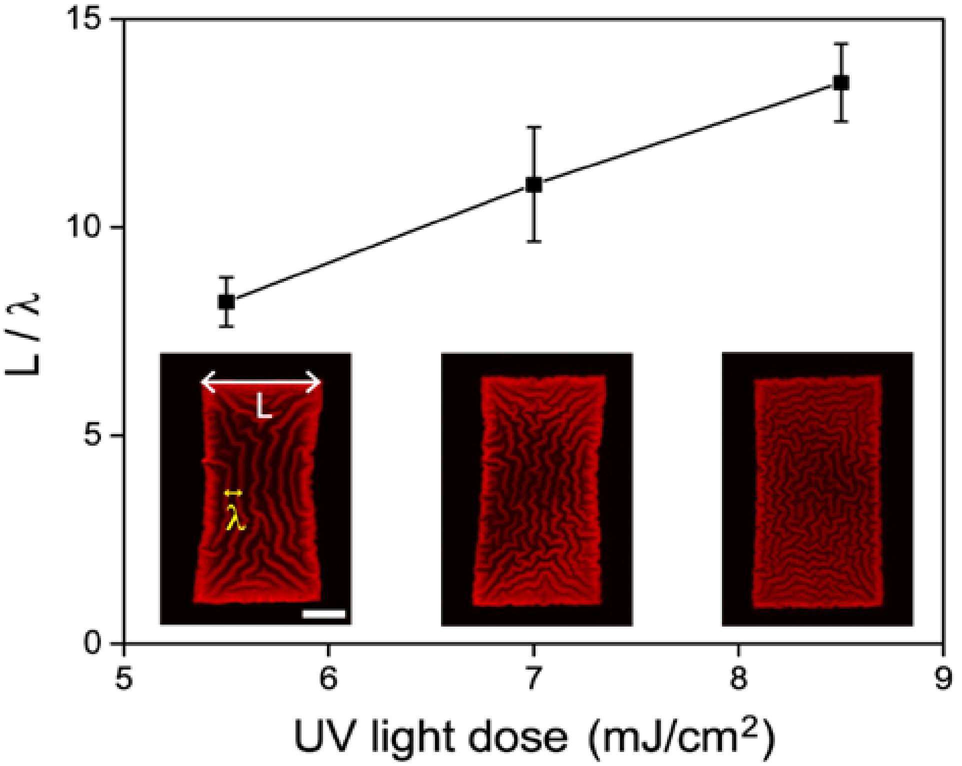

Figure 4.2 Control of orientation randomness by changing the ratio of the short side length to the wavelength in anisotropic shape of microparticles (scale bar: 25 µm). Data at each point were obtained from 10 wrinkled microparticles. The average value was 8.21, 11.03, and 13.47, respectively. The error bars represent the standard deviation, 0.59, 1.37, and 0.94, respectively [74].

We then tried to control and increase the pattern randomness in anisotropic particles, specifically in rectangles that showed a relatively low level of orientation randomness compared to the isotropic circular particles. For this purpose, we tuned the ratio of the short side length to the characteristic wavelength (L/λ) as a dimension parameter (Figure 4.2). As shown in the graph, the degree of randomness increased as the L/λ increased. The tuning of L/λ value was achieved by changing the λ while maintaining the particle size (L) to a specific value. As explained in section 3.3, the characteristic wavelength value was controlled by changing the UV light dose for the photopolymerization of the microparticles. The higher UV light dose resulted in a smaller wavelength due to the increased crosslinking density and elastic modulus in the polymer substrate, and thus a larger L/λ value. Therefore, we could provide random ridge patterns to some degree in microparticles with shape anisotropy, by controlling the L/λ value.

In addition to the randomness, we could control the orientation of wrinkles to a particular direction by designing the internal structure of the particle. For this purpose, we fabricated holes in microparticles in order to direct ridges toward the hole (Figure 4.3). When the hole was located at the particle center, ridges were patterned with radial direction compared to the regular particle without a hole. In contrast, when the hole was not located in the center region, some ridges at the opposite side of the hole were not guided and exhibited random orientations. When there were more than two holes, including the hole-array, ridges between holes were connected in straight lines. These results were very similar to the wrinkle patterns controlled by pre-patterned substrates with bas-relief structures [10, 11]. In summary, despite the random nature of the wrinkles, we could control the level of randomness of wrinkle patterns by designing the particle shape or the dimension parameters. Moreover, we could align ridges to a specific direction by punching holes on the microparticle.

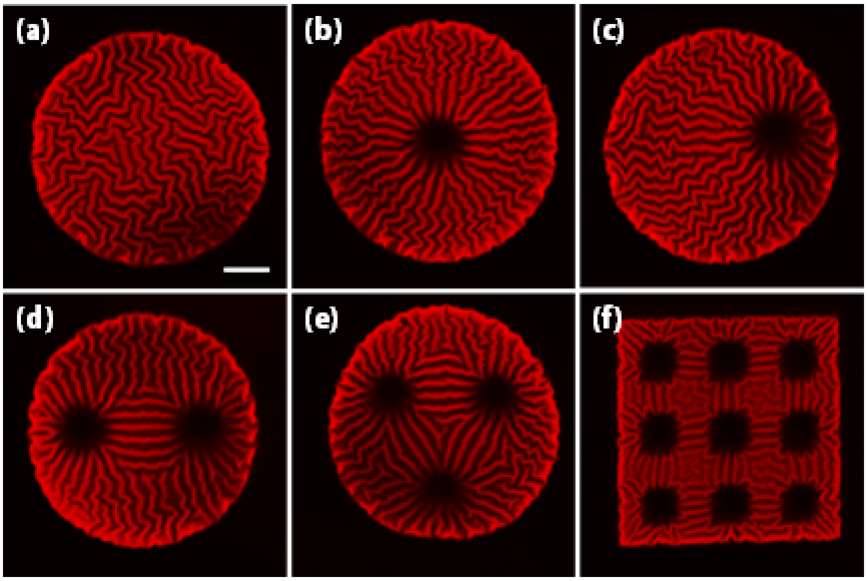

Figure 4.3 Control of ridge orientation using internal hole structures: (a) Without hole; (b) One hole at the particle center; (c) One hole at the off-center region; (d) Two holes; (e) Three holes; (f) Holes with an array pattern.

4.2 Sophisticated Control Method: Guided Wrinkling

We presented several simple, controllable wrinkle patterning techniques in the previous section. However, they still lack elaborate ridge control mechanisms, such as control of the ridge orientation to any intended direction in an individual ridge level. Therefore, the generable wrinkle patterns were restricted to similar outcomes achievable by other previously developed patterning methods. To increase the flexibility of the patterning with wrinkles, and consequently expand the application field of the wrinkling-based patterning, we developed a novel wrinkle control method based on guided wrinkling.

In the guided wrinkling, we utilized the ridge guiding structures in order to align ridges to specific directions. The overall process of the guided wrinkling is shown in Figure 4.4. First, we pre-patterned the guiding structures on one surface of the microparticle during the photopolymerization process. The guiding structure was fabricated as an organization of small grooves by blocking the UV light on specific sites using 1 by 1 pixel size black dots in the photomask (Figure 4.4(a)). These grooves were only patterned on the surface where the photopolymerization of the particle first occurred by precisely focusing the UV light on that layer. As an example, we pre-patterned groove arrays with a checkerboard pattern. The cross-section view shows the patterned grooves on the top surface (Figure 4.4(b)). Then, we coated these pre-patterned microparticles with silica and dried them to induce wrinkling on the particle surface. During this wrinkling process, the ridges were

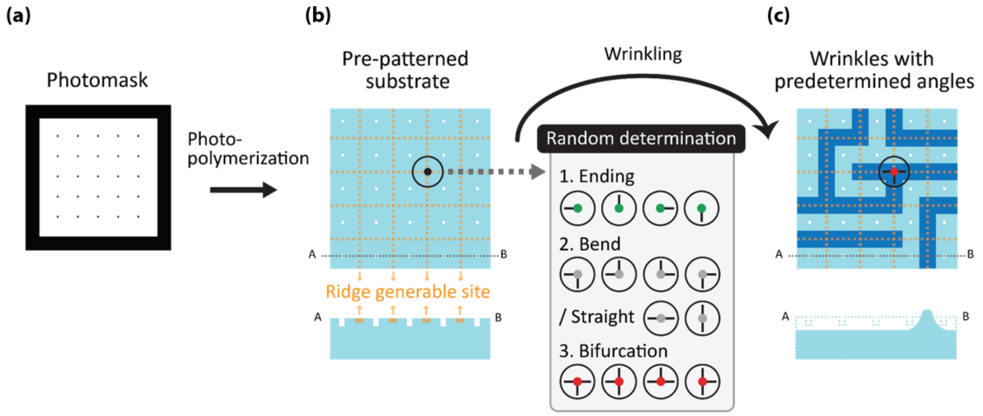

Figure 4.4 Schematic illustration of the whole process for controlled wrinkle patterning using ridge guiding structures.

generable only outside the guiding grooves (orange dash lines in the Figure 4.4(b)) because the grooves could only be transformed into valleys, not into ridges. As a result, the ridges were generated with orthogonal directionality (dark blue lines in the Figure 4.4(c)). In other words, we could control the orientation of ridges by changing the geometry of the ridge guiding structures or the arrangement of groove arrays.

Interestingly, although we could control the ridge orientation using the guiding structure, the type of ridge (ridge ending, bend, straight line, or bifurcation) at each ridge decision-point was randomly determined due to the intrinsic random nature of wrinkling. For example, a ridge decision-point depicted in Figure 4.4(b) was converted to the ridge bifurcation after wrinkling. As a result, even wrinkled microparticles with the same guiding structures showed different wrinkle patterns while maintaining the overall orthogonal directionality.

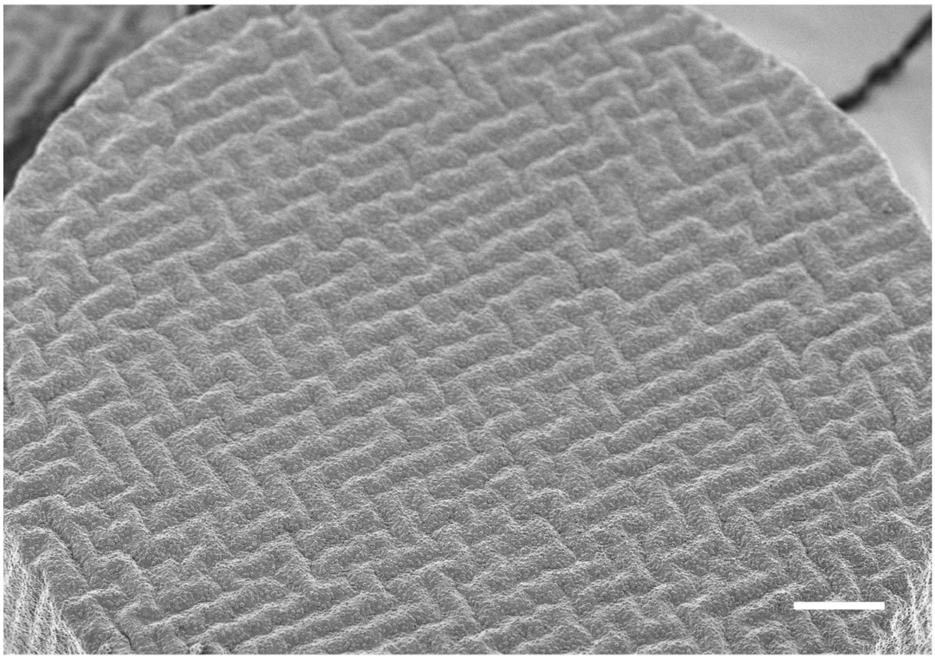

Figure 4.5 SEM image of a wrinkled microparticle with orthogonally guided wrinkle patterns (scale bar: 10 μm) [75].

When we observed the fabricated wrinkled microparticles using SEM, we verified highly uniform ridge patterns with controlled directionality throughout the entire particle surface (Figure 4.5). In addition, when we imaged using CLSM, the ridge patterns were not observed in pre-patterned particles (Figure 4.6(a)). However, the wrinkle patterns were clearly imaged after wrinkling the pre-patterned microparticles (Figure 4.6(b)). This verified that the controlled ridge patterns were spontaneously generated by mechanical instability, not by the direct patterning with photolithography. Overall, the presented programmable wrinkle patterning method provides simple, but powerful design strategy for controlled wrinkle patterns by requiring only corresponding photomask for the guiding structure, without any external devices for the stress control or additional chemical processes.

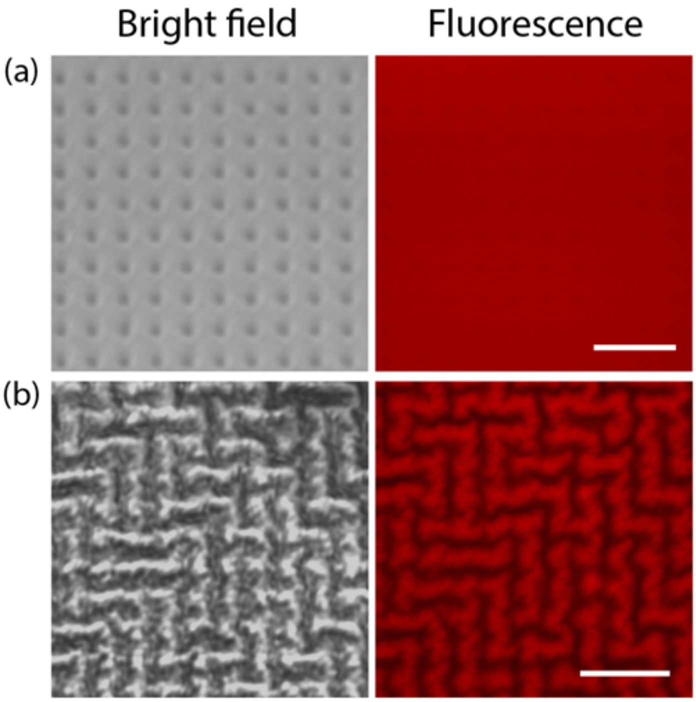

Figure 4.6 CLSM images of surfaces before and after wrinkling: (a) Before wrinkling. The pre-patterned microparticle was immersed in ethanol for imaging (scale bar: 10 μm); (b) After wrinkling. The wrinkled microparticle was in the air condition after drying for imaging (scale bar: 10 μm) [75].

4.3 Analysis of Orthogonal Ridge Patterns

In this section, the organizing principle of the orthogonal wrinkle patterns will be briefly discussed by comparing the experimental results to the computational simulation results. For this purpose, we assumed several hypothesis models for the ridge formation based on the probability of the ridge type determination at each ridge decision-point. Then, we generated artificial patterns consisting of orthogonal straight lines (visualization of ridges) according to these models, and compared them to experimentally fabricated patterns. Also, the control of the ridge density in this orthogonal pattern will be demonstrated.

First, we performed an additional image processing process to extract orthogonal ridge patterns with straight lines from the original CLSM images. We introduced this process for more precise extraction of ridge information and thus for a reliable comparative analysis with simulated patterns. To transform imperfect ridge lines (“analog”) into perfect straight lines (“digital”) in the CLSM images, we utilized the Hough transform method that is generally adapted to detect straight lines from the given features (Figure 4.7). After converting the original CLSM image to the binary image, we detected straight lines from all ridges by applying the Hough transform, and defined the length of each straight line by multiplying the transform result with the binary image. Then, for every crossing points (the intersection between the vertical lines and the horizontal lines), the adjacent two cross points were connected if they were in the same ridge in the binary image. As a result, we were able to obtain digitized 2D line patterns. Finally, we extracted minutia information (ridge endings, bifurcations, bends, straight lines) using these digitized images from the 20 different wrinkled microparticles (Figure 4.8(a)). Here, we utilized central 16 by 16 lines as the minutia extraction area, and applied the same size in the following simulations.

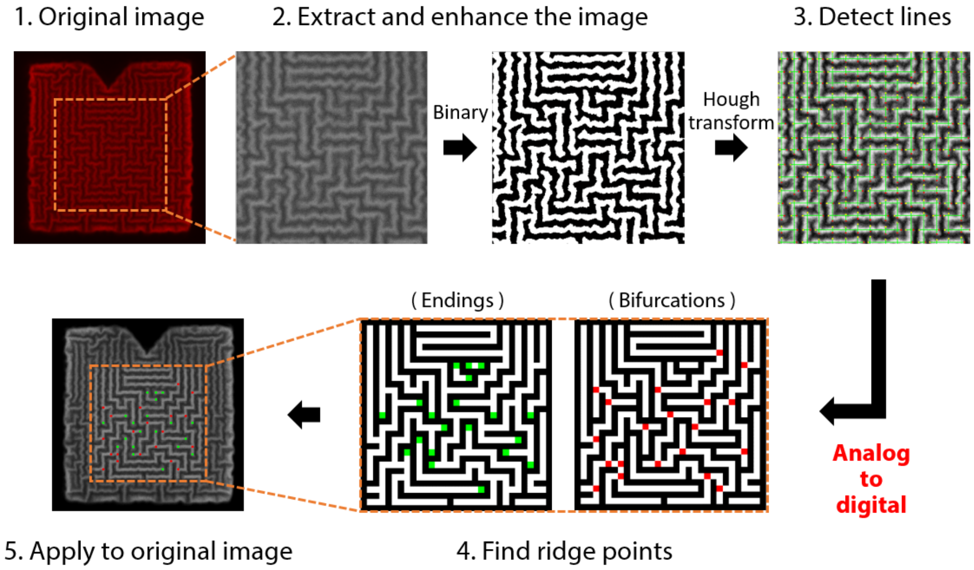

Figure 4.7 Analog to digital conversion process of orthogonally guided ridges for the reliable ridge analysis.

Next, we generated this kind of line patterns using two model algorithms. In the first model, the probability of the ridge type resulting in either an ending, a bend, a straight line, or a bifurcation was assumed as the same value (0.25) at every ridge

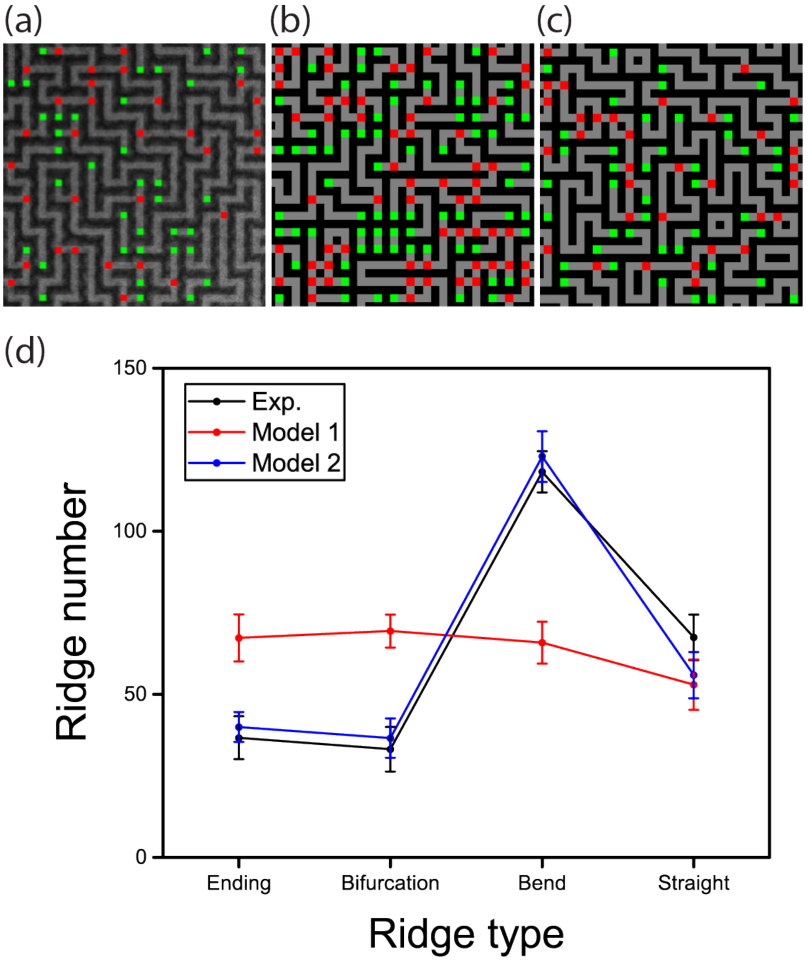

Figure 4.8 Comparative analysis of the orthogonal ridge pattern in different generation methods: (a) Experimental results; (b) Even probability model; (c) Modified probability model; (d) Distribution of the ridge number at each ridge type. Each data point was obtained from 20 ridge patterns. The error bars represent the standard deviation of the ridge number.

Table 4.1 Conditions for even and modified probability models

Model	Ending	Bifurcation	Bend	Straight
1. Even probability	0.25	0.25	0.25	0.25
2. Modified probability	0.1434	0.1295	0.4617	0.2635

decision-point (Even probability, Table 4.1). In addition, by observing the wrinkling moment using the confocal microscope, we found that the ridge determination occurred first at the first dried region, usually at the edge of the microparticles, and spread to neighboring regions. Reflecting this observation, we assumed that the ridge generation began at the farthest points from the pattern center and spread to the center in a concentric manner by satisfying boundary conditions to neighboring regions with the designated probabilities. We then simulated 20 times and obtained minutia information from these different patterns (Figure 4.8 (b)).

In the second model, we utilized different determination probabilities for each ridge type (Table 4.1). These probabilities were derived from previously analyzed experimental data by considering the proportion of the ridge endings, bifurcations, bends, and straight lines in the total accumulated number of ridge types. The reason that the sum of these probabilities were less than one was that there was another ridge type, an island (isolated dot), in experimentally fabricated patterns. However, we ignored this island type because the number of the cases was extremely low compared to that of others. We then inversely used this probability distribution for simulating the orthogonal patterns (Figure 4.8(c)).

The graph in Figure 4.8(d) summarizes the distribution of the number of ridge types in each group. When we compared the experimental result to the model 1, we could conclude that the orthogonal ridge patterns were determined by biased probabilities rather than by completely random processes. Moreover, although the number distribution was nearly the same between the experimental result and the model 2, the pattern architecture was slightly different. The simulation model showed a few closed-loop patterns, while the experimental result hardly showed them. From this observation, we could also conclude that there were some other factors to determining the overall ridge patterns, like existence of energetically unfavorable patterns, in addition to the probability.

The presented ridge analysis process based on the ridge digitization is also useful as a decoding method when we utilize the orthogonal ridge patterns as topographical codes like the artificial fingerprint. Because digitized ridge images did not contain ambiguous ridge lines that could be detected as unintended minutia points in error, we could reduce decoding errors. For example, we verified that the security level and code capacity could be easily tuned in orthogonal wrinkle patterns by changing the interval between the guiding grooves (Figure 4.9). Compared to artificial fingerprints, these highly periodic structures provided more obvious classifications of the security level when we extracted minutia density information after digitizing the original CLSM images. The decoding process based on the digitized pattern also provided a robust code-reading system.

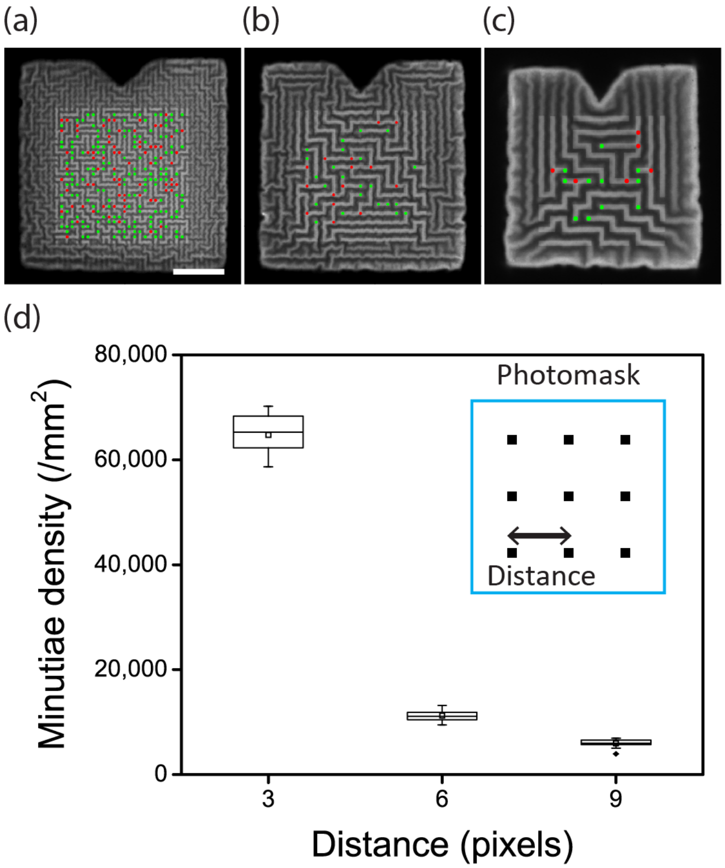

Figure 4.9 Control of the ridge density in the orthogonal wrinkle pattern: (a-c) Representative images of the wrinkled microparticle with different guiding structure dimension. The green and red dots show ridge endings and bifurcations, respectively (scale bar: 25 μm); (b) Minutia density distribution according to the guiding structure dimension.

4.4 Programming Ridge Directionality

Thus far, we have demonstrated the generation of orthogonal ridges throughout the entire microparticle surface using the guiding groove array with the checkerboard pattern. By modifying the architecture of the guiding structure, we were able to expand the diversity of controlled wrinkle patterns with the arbitrary direction.

First, we achieved self-organization of unidirectionally and hexagonally aligned ridge patterns by changing the arrangement of groove arrays for the guiding structure. For the highly anisotropic ridge pattern, we decreased the distance between the grooves along one axis from the checkerboard pattern, and consequently confined the individual ridge along the guiding structure (Figure 4.10(a)). To verify the controllability and reproducibility of the programmed patterns based on this control mechanism, we analyzed the distribution of ridge orientation accumulated from 20 microparticles. In this analysis, we did not use the digitizing process, but extracted the ridge orientation from the gray scale images. The peak values were clearly observed near 90 degrees for the anisotropic patterns (Figure 4.10(d)) and near 90 and 180 degrees for the orthogonal patterns (Figure 4.10(e)), which verified that the programmed wrinkle patterns were fabricated with reliable reproducibility. Interestingly, the anisotropic wrinkles could usually be generated by means of mechanical clamps in order to apply uniaxial stress to samples. However, our ridge guiding structure allowed the simple generation of highly anisotropic patterns through the isotropic shrinking process, without any external devices.

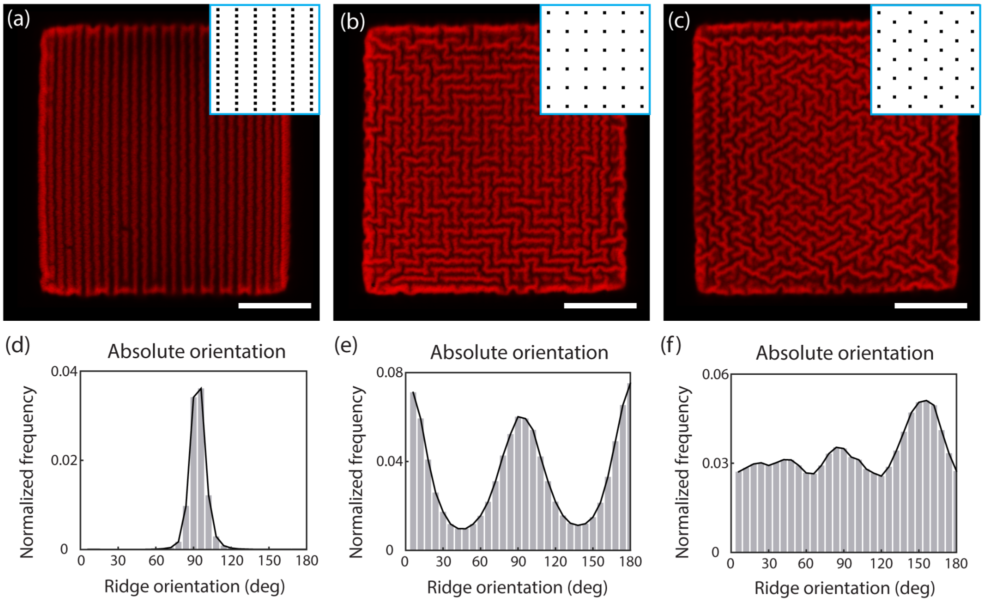

Figure 4.10 Control of ridge orientation: (a-c) Representative CLSM image of a unidirectionally, an orthogonally, and a hexagonally ordered wrinkle pattern, respectively. The inset image represent design of the photomask corresponding to the pattern (scale bars: 25 μm); (d-f) Distribution of the ridge orientation in unidirectional, orthogonal, and hexagonal wrinkle patterns. Each histogram was obtained from 20 microparticles [75].

Moreover, we modified the groove array arrangement to form a hexagonal shape (Figure 4.10(c)). The ridges were intended to align along 30, 90, and 150 degree directions. However, the hexagonal ridge patterns showed rather indistinct peak values in the orientation histogram, compared to the orthogonal patterns (Figure 4.10(f)). We believe this resulted from higher complexity in the process determining the ridge types at the ridge decision-point, because the hexagonal shape possessed one more orientation degree of freedom and two more kinds of ridge decision-points than the orthogonal shape.

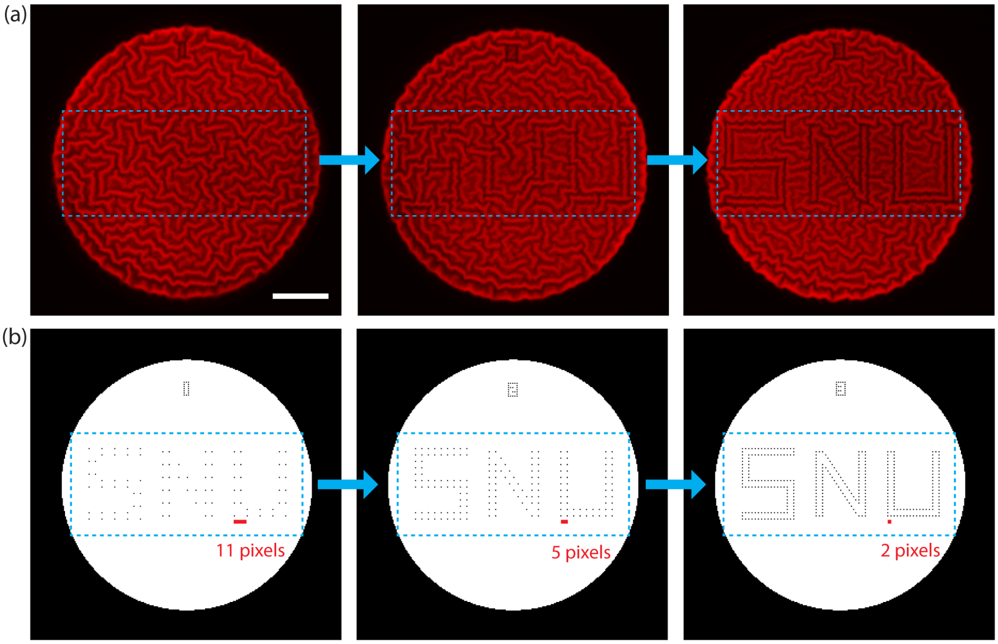

Figure 4.11 Inscribing letters with ridges: (a) CLSM images of wrinkled microparticles with programmed patterns (scale bar: 25 μm); (b) Corresponding photomasks [75].

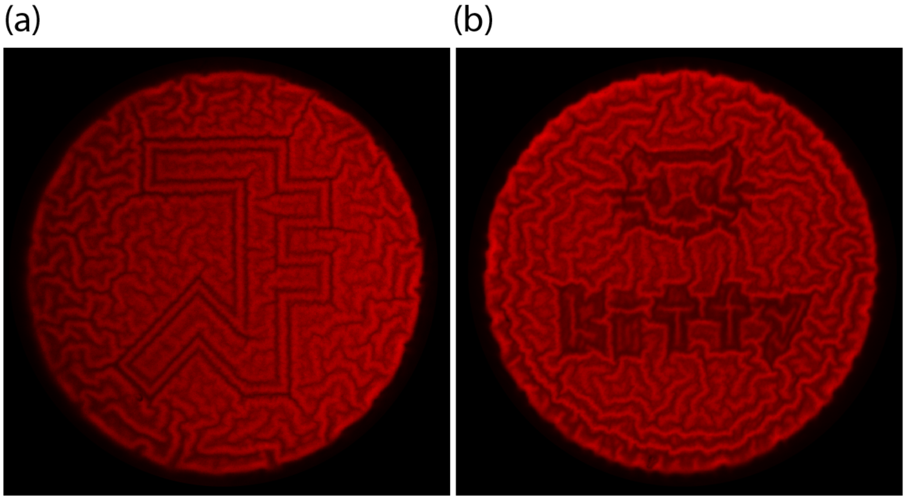

Figure 4.12 Examples of flexible patterning with wrinkles: (a) Patterning Seoul National University symbol; (b) Patterning “Hello Kitty” symbol.

Second, by expanding the guiding structure over the array architecture, we could fabricate ridge patterns with arbitrary shapes. As an example, we wrote letters with wrinkles on the surface of microparticles (Figure 4.11). The photomask for the guiding structure was designed using letter shapes with different inter-groove distances (Figure 4.11(b)). The letter pattern in the programmed region then became clear as the inter-groove distance decreased, and the other region showed uncontrolled random patterns (Figure 4.11(a)).

Furthermore, we demonstrated the patterning of specific symbols with wrinkles (Figure 4.12). The sophisticated wrinkle control and flexible pattern design was possible using the direct wrinkle patterning methods with lasers or FIB [19, 20]. However, our patterning approach can simultaneously generate random wrinkle patterns with the programmed patterns. These heterogeneously patterned microparticles can be applied as microtaggants for anti-counterfeiting purposes because they can provide additional information with easily differentiable patterns, as well as unclonable properties like the artificial fingerprint.

In summary, we developed various wrinkle control methods on the microparticle substrate. We were able to roughly control the level of randomness with the particle shape or the wavelength to the particle size ratio in anisotropic particles. To handle random wrinkles with a high degree of flexibility, we pre-patterned the designed ridge guiding structure on the particle substrate and controlled the ridge orientation based on the geometry of this guiding structure. The highly regular and periodic wrinkle patterns with orthogonal directionality were generated by pre-patterning guiding grooves with a checkerboard pattern. These kind of orthogonal ridge patterns were then analyzed after transforming original curved ridges into perfect straight lines, which can reduce decoding errors of the ridge patterns. Furthermore, we demonstrated ridge orientation control to any direction by confining individual ridges inside the guiding structure. We expect the presented elaborate self-organization approach would extend to applications of wrinkled microstructures in various fields due to its flexible pattern design scheme.

Chapter 5

Conclusion

In this dissertation, a wrinkle patterning technology on microparticle-based substrates was presented. First, random wrinkles were patterned on the surface of the inelastic silica film covering an elastic polymeric substrate using biaxial in-plane stress. These wrinkled microparticles were then applied to the microtaggant-based anti-counterfeiting strategy as artificial microfingerprints. The unclonability and high level of individuality of the artificial fingerprints provided a powerful authentication system similar to PUF, and the reliable decoding process was provided by utilizing conventional fingerprint identification algorithms. Flexible code control mechanisms were also achieved in terms of the security level, the code capacity, and additional information for the taggant classification, by tuning the wavelength of the wrinkle pattern or the particle shape. The entire authentication process and the stability of the artificial fingerprint system integrated on the products were then demonstrated. In this study, the randomness of wrinkle patterns was functionalized for the first time, and a new axis of security application was provided to wrinkle patterning. Irreplicable anti-counterfeiting strategies such as our biomimetic microfingerprints could become excellent solutions to the trillion-dollar counterfeit market. Additionally, the stochastic wrinkle patterns as fingerprint analogs could inspire researchers in wrinkle patterning applications and provide experimental tools to resolve unproven theories in morphological instabilities and fingerprint generation studies.

Next, controlled wrinkle patterning methods were developed to expand application fields of the bottom-up based patterning technology. Random wrinkles were roughly controlled in terms of the orientational randomness of ridges through particle geometries or the dimension ratio between the wavelength and the particle shape. Beyond these basic approaches, the sophisticated control mechanism was developed using the ridge guiding structure. By designing the arrangement of the guiding grooves, the periodic, ordered, but random patterns were generated. Moreover, the single ridges to any direction were able to be generated by confining them inside the guiding structure.

For future work, the long-term stability of the artificial fingerprint can be tested in terms of pattern conservation in order to realize commercial applications. Also, the length scale of the wrinkle pattern can be reduced from microscale to nanoscale with the goal of expanding applications of the wrinkled microparticles to different fields, including optics, the behavioral study of cells or microorganisms, and anti-counterfeiting. Moreover, although this dissertation focused on the polymeric microparticle substrate, the presented guided wrinkling approach can be generalized to various materials or substrate systems, in order to increase its practicality. Ultimately, the technology described here will inspire researchers developing transformation methods of 2D structures into 3D structures as well as those studying mechanical instabilities.

Bibliography

[1] H. G. Allen, *Analysis and Design of Structural Sandwich Panels*. New York: Pergamon, 1969.

[2] S. P. Timoshenko, *Theory of elastic stability*. New York: McGraw-Hill, 1988.

[3] J. Groenewold, "Wrinkling of plates coupled with soft elastic media," *Physica A: Statistical Mechanics and its Applications,* vol. 298, no. 1–2, pp. 32-45, 2001.

[4] E. Cerda and L. Mahadevan, "Geometry and Physics of Wrinkling," *Physical Review Letters,* vol. 90, no. 7, p. 074302, 2003.

[5] X. Chen and J. W. Hutchinson, "Herringbone Buckling Patterns of Compressed Thin Films on Compliant Substrates," *Journal of Applied Mechanics,* vol. 71, no. 5, pp. 597-603, 2004.

[6] X. Chen and J. Yin, "Buckling patterns of thin films on curved compliant substrates with applications to morphogenesis and three-dimensional micro-fabrication," *Soft Matter,* vol. 6, no. 22, pp. 5667-5680, 2010.

[7] J. Genzer and J. Groenewold, "Soft matter with hard skin: From skin wrinkles to templating and material characterization," *Soft Matter,* vol. 2, no. 4, pp. 310-323, 2006.

[8] S. Yang, K. Khare, and P.-C. Lin, "Harnessing Surface Wrinkle Patterns in Soft Matter," *Advanced Functional Materials,* vol. 20, no.

16, pp. 2550-2564, 2010.

[9] D. Breid and A. J. Crosby, "Effect of stress state on wrinkle morphology," *Soft Matter,* vol. 7, no. 9, pp. 4490-4496, 2011.

[10] N. Bowden, S. Brittain, A. G. Evans, et al., "Spontaneous formation of ordered structures in thin films of metals supported on an elastomeric polymer," *Nature,* vol. 393, no. 6681, pp. 146-149, 1998.

[11] N. Bowden, W. T. S. Huck, K. E. Paul, et al., "The controlled formation of ordered, sinusoidal structures by plasma oxidation of an elastomeric polymer," *Applied Physics Letters,* vol. 75, no. 17, pp. 2557-2559, 1999.

[12] D. B. H. Chua, H. T. Ng, and S. F. Y. Li, "Spontaneous formation of complex and ordered structures on oxygen-plasma-treated elastomeric polydimethylsiloxane," *Applied Physics Letters,* vol. 76, no. 6, pp. 721-723, 2000.

[13] W. T. S. Huck, N. Bowden, P. Onck, et al., "Ordering of Spontaneously Formed Buckles on Planar Surfaces," *Langmuir,* vol. 16, no. 7, pp. 3497-3501, 2000.

[14] C.-M. Chen, J. C. Reed, and S. Yang, "Guided wrinkling in swollen, pre-patterned photoresist thin films with a crosslinking gradient," *Soft Matter,* vol. 9, no. 46, pp. 11007-11013, 2013.

[15] Q. Du, Y. Guan, X. X. Zhu, et al., "Swelling-induced surface instability patterns guided by pre-introduced structures," *Soft Matter,* vol. 11, no. 10, pp. 1937-1944, 2015.

[16] P.-C. Lin and S. Yang, "Spontaneous formation of one-dimensional ripples in transit to highly ordered two-dimensional herringbone structures through sequential and unequal biaxial mechanical stretching," *Applied Physics Letters,* vol. 90, no. 24, pp. 241903-3, 2007.

[17] C.-C. Fu, A. Grimes, M. Long, et al., "Tunable Nanowrinkles on Shape Memory Polymer Sheets," *Advanced Materials,* vol. 21, no. 44, pp. 4472-4476, 2009.

[18] E. Lee, M. Zhang, Y. Cho, et al., "Tilted Pillars on Wrinkled Elastomers as a Reversibly Tunable Optical Window," *Advanced Materials,* vol. 26, no. 24, pp. 4127-4133, 2014.

[19] M.-W. Moon, S. H. Lee, J.-Y. Sun, et al., "Wrinkled hard skins on polymers created by focused ion beam," *Proceedings of the National Academy of Sciences,* vol. 104, no. 4, pp. 1130-1133, 2007.

[20] C. F. Guo, V. Nayyar, Z. Zhang, et al., "Path-Guided Wrinkling of Nanoscale Metal Films," *Advanced Materials,* vol. 24, no. 22, pp. 3010-3014, 2012.

[21] P. J. Yoo, K. Y. Suh, S. Y. Park, et al., "Physical Self-Assembly of Microstructures by Anisotropic Buckling," *Advanced Materials,* vol. 14, no. 19, pp. 1383-1387, 2002.

[22] P. J. Yoo and H. H. Lee, "Complex Pattern Formation by Adhesion-Controlled Anisotropic Wrinkling," *Langmuir,* vol. 24, no. 13, pp. 6897-6902, 2008.

[23] M. Guvendiren, S. Yang, and J. A. Burdick, "Swelling-Induced Surface Patterns in Hydrogels with Gradient Crosslinking Density," *Advanced Functional Materials,* vol. 19, no. 19, pp. 3038-3045, 2009.

[24] S. J. Ma, S. J. Mannino, N. J. Wagner, et al., "Photodirected Formation and Control of Wrinkles on a Thiol–ene Elastomer," *ACS Macro Letters,* vol. 2, no. 6, pp. 474-477, 2013.

[25] N. Stoop, R. Lagrange, D. Terwagne, et al., "Curvature-induced symmetry breaking determines elastic surface patterns," *Nature Materials,* vol. 14, no. 3, pp. 337-342, 2015.

[26] J. Yin, Z. Cao, C. Li, et al., "Stress-driven buckling patterns in spheroidal core/shell structures," *Proceedings of the National Academy of Sciences,* vol. 105, no. 49, pp. 19132-19135, 2008.

[27] J. Yin, G. J. Gerling, and X. Chen, "Mechanical modeling of a wrinkled fingertip immersed in water," *Acta Biomaterialia,* vol. 6, no. 4, pp. 1487-1496, 2010.

[28] G. Cao, X. Chen, C. Li, et al., "Self-Assembled Triangular and

Labyrinth Buckling Patterns of Thin Films on Spherical Substrates," *Physical Review Letters,* vol. 100, no. 3, p. 036102, 2008.

[29] J. Yin, E. Bar-Kochba, and X. Chen, "Mechanical self-assembly fabrication of gears," *Soft Matter,* vol. 5, no. 18, pp. 3469-3474, 2009.

[30] A. C. Trindade, J. P. Canejo, L. F. V. Pinto, et al., "Wrinkling Labyrinth Patterns on Elastomeric Janus Particles," *Macromolecules,* vol. 44, no. 7, pp. 2220-2228, 2011.

[31] D. Breid and A. J. Crosby, "Curvature-controlled wrinkle morphologies," *Soft Matter,* vol. 9, no. 13, pp. 3624-3630, 2013.

[32] M. Li, N. Hakimi, R. Perez, et al., "Microarchitecture for a Three-Dimensional Wrinkled Surface Platform," *Advanced Materials,* vol. 27, no. 11, pp. 1880-1886, 2015.

[33] X. Jiang, S. Takayama, X. Qian, et al., "Controlling Mammalian Cell Spreading and Cytoskeletal Arrangement with Conveniently Fabricated Continuous Wavy Features on Poly(dimethylsiloxane)," *Langmuir,* vol. 18, no. 8, pp. 3273-3280, 2002.

[34] M. Guvendiren and J. A. Burdick, "The control of stem cell morphology and differentiation by hydrogel surface wrinkles," *Biomaterials,* vol. 31, no. 25, pp. 6511-6518, 2010.

[35] A. Chen, D. K. Lieu, L. Freschauf, et al., "Shrink-Film Configurable Multiscale Wrinkles for Functional Alignment of Human Embryonic Stem Cells and their Cardiac Derivatives," *Advanced Materials,* vol. 23, no. 48, pp. 5785-5791, 2011.

[36] C. Harrison, C. M. Stafford, W. Zhang, et al., "Sinusoidal phase grating created by a tunably buckled surface," *Applied Physics Letters,* vol. 85, no. 18, pp. 4016-4018, 2004.

[37] E. P. Chan and A. J. Crosby, "Fabricating Microlens Arrays by Surface Wrinkling," *Advanced Materials,* vol. 18, no. 24, pp. 3238-3242, 2006.

[38] C. M. Stafford, C. Harrison, K. L. Beers, et al., "A buckling-based metrology for measuring the elastic moduli of polymeric thin films,"

Nature Materials, vol. 3, no. 8, pp. 545-550, 2004.

[39] K. Efimenko, M. Rackaitis, E. Manias, et al., "Nested self-similar wrinkling patterns in skins," *Nature Materials,* vol. 4, no. 4, pp. 293-297, 2005.

[40] M. Pretzl, A. Schweikart, C. Hanske, et al., "A Lithography-Free Pathway for Chemical Microstructuring of Macromolecules from Aqueous Solution Based on Wrinkling," *Langmuir,* vol. 24, no. 22, pp. 12748-12753, 2008.

[41] K. Efimenko, J. Finlay, M. E. Callow, et al., "Development and Testing of Hierarchically Wrinkled Coatings for Marine Antifouling," *ACS Applied Materials & Interfaces,* vol. 1, no. 5, pp. 1031-1040, 2009.

[42] E. P. Chan, E. J. Smith, R. C. Hayward, et al., "Surface Wrinkles for Smart Adhesion," *Advanced Materials,* vol. 20, no. 4, pp. 711-716, 2008.

[43] Y. Sun, W. M. Choi, H. Jiang, et al., "Controlled buckling of semiconductor nanoribbons for stretchable electronics," *Nature Nanotechnology,* vol. 1, no. 3, pp. 201-207, 2006.

[44] D.-H. Kim, J.-H. Ahn, W. M. Choi, et al., "Stretchable and Foldable Silicon Integrated Circuits," *Science,* vol. 320, no. 5875, pp. 507-511, 2008.

[45] H. J. Bae, S. Bae, C. Park, et al., "Biomimetic Microfingerprints for Anti-Counterfeiting Strategies," *Advanced Materials,* vol. 27, no. 12, pp. 2083-2089, 2015.

[46] S. E. Chung, W. Park, H. Park, et al., "Optofluidic maskless lithography system for real-time synthesis of photopolymerized microstructures in microfluidic channels," *Applied Physics Letters,* vol. 91, no. 4, p. 041106, 2007.

[47] J. Ge and Y. Yin, "Magnetically Tunable Colloidal Photonic Structures in Alkanol Solutions," *Advanced Materials,* vol. 20, no. 18, pp. 3485-3491, 2008.

[48] W. Stöber, A. Fink, and E. Bohn, "Controlled growth of monodisperse silica spheres in the micron size range," *Journal of Colloid and Interface Science,* vol. 26, no. 1, pp. 62-69, 1968.

[49] L. N. Kim, M. Kim, K. Jung, et al., "Shape-encoded silica microparticles for multiplexed bioassays," *Chemical Communications,* vol. 51, no. 60, pp. 12130-12133, 2015.

[50] J. Yin and M. C. Boyce, "Materials science: Unique wrinkles as identity tags," *Nature,* vol. 520, no. 7546, pp. 164-165, 2015.

[51] Dennemeyer Takes the Counterfeit Fight to the Next Generation, *www.businesswire.com/news/home/20131212005527/en/Dennemeyer-Takes-Counterfeit-Fight-Generation#.VVxTSmCaGdi*

[52] The Economy of Counterfeit Drugs [Info-graphic], *http://carrington.edu/blog/medical/the-economy-of-counterfeit-drugs-infographic/*

[53] Fake drugs risk patient's lives, *www.novartis.com/newsroom/feature-stories/2014/03/fighting-pharmaceutical-crime.shtml*

[54] A small matter of authenticity, *http://www.manufacturingchemist.com/news/article_page/A_small_matter_of_authenticity/57516*

[55] H. Lee, J. Kim, H. Kim, et al., "Colour-barcoded magnetic microparticles for multiplexed bioassays," *Nature Materials,* vol. 9, no. 9, pp. 745-749, 2010.

[56] J. Lee, P. W. Bisso, R. L. Srinivas, et al., "Universal process-inert encoding architecture for polymer microparticles," *Nature Materials,* vol. 13, no. 5, pp. 524-529, 2014.

[57] S. Han, H. J. Bae, J. Kim, et al., "Lithographically Encoded Polymer Microtaggant Using High-Capacity and Error-Correctable QR Code for Anti-Counterfeiting of Drugs," *Advanced Materials,* vol. 24, no. 44, pp. 5924-5929, 2012.

[58] K. Braeckmans, S. C. De Smedt, C. Roelant, et al., "Encoding microcarriers by spatial selective photobleaching," *Nature Materials,*

vol. 2, no. 3, pp. 169-173, 2003.

[59] C. Huang, B. Lucas, C. Vervaet, et al., "Unbreakable Codes in Electrospun Fibers: Digitally Encoded Polymers to Stop Medicine Counterfeiting," *Advanced Materials,* vol. 22, no. 24, pp. 2657-2662, 2010.

[60] R. Maes and I. Verbauwhede, "Physically Unclonable Functions: A Study on the State of the Art and Future Research Directions," in *Towards Hardware-Intrinsic Security*, A.-R. Sadeghi and D. Naccache, Eds., ed: Springer Berlin Heidelberg, 2010, pp. 3-37.

[61] R. Pappu, B. Recht, J. Taylor, et al., "Physical One-Way Functions," *Science,* vol. 297, no. 5589, pp. 2026-2030, 2002.

[62] J. D. R. Buchanan, R. P. Cowburn, A.-V. Jausovec, et al., "Forgery: `Fingerprinting' documents and packaging," *Nature,* vol. 436, no. 7050, pp. 475-475, 2005.

[63] J. Kim, J. M. Yun, J. Jung, et al., "Anti-counterfeit nanoscale fingerprints based on randomly distributed nanowires," *Nanotechnology,* vol. 25, no. 15, p. 155303, 2014.

[64] P. Tuyls, G.-J. Schrijen, B. Škorić, et al., "Read-Proof Hardware from Protective Coatings," in *Cryptographic Hardware and Embedded Systems - CHES 2006*. vol. 4249, L. Goubin and M. Matsui, Eds., ed: Springer Berlin Heidelberg, 2006, pp. 369-383.

[65] Z. Hu, J. M. M. L. Comeras, H. Park, et al., "Physically unclonable cryptographic primitives using self-assembled carbon nanotubes," *Nature Nanotechnology,* vol. 11, no. 6, pp. 559-565, 2016.

[66] Q. Xiao and H. Raafat, "Fingerprint image postprocessing: A combined statistical and structural approach," *Pattern Recognition,* vol. 24, no. 10, pp. 985-992, 1991.

[67] Y. Yin, Y. Lu, Y. Sun, et al., "Silver Nanowires Can Be Directly Coated with Amorphous Silica To Generate Well-Controlled Coaxial Nanocables of Silver/Silica," *Nano Letters,* vol. 2, no. 4, pp. 427-430, 2002.

[68] S. Bae, *Artificial micro fingerprint for authentication and anticounterfeiting applications*, M.S. Thesis, Interdisciplinary Program for Bioengineering, Seoul National University, August 2014.

[69] A. Arakala, J. Jeffers, and K. J. Horadam, "Fuzzy Extractors for Minutiae-Based Fingerprint Authentication," in *Advances in Biometrics*. vol. 4642, S.-W. Lee and S. Li, Eds., ed: Springer Berlin Heidelberg, 2007, pp. 760-769.

[70] R. Cappelli, "Fingerprint Sample Synthesis," in *Encyclopedia of Biometrics*, ed: Springer, 2009, pp. 513-523.

[71] R. Cappelli, D. Maio, and D. Maltoni, "Synthetic fingerprint-database generation," *Object recognition supported by user interaction for service robots*, 2002, pp. 744-747 vol.3.

[72] D. Maltoni, D. Maio, A. K. Jain, et al., *Handbook of fingerprint recognition*. Springer, 2009.

[73] N. K. Ratha and R. Bolle, *Automatic fingerprint recognition systems*. Springer, 2004.

[74] H. Bae, S. Bae, C. Park, et al., "Wrinkiled microparticles for unclonable microtaggants," in *Proc. of The 18th International Conference on Solid-State Sensors, Actuators and Microsystems*, Alaska, USA, June 21-25, 2015, pp. 768-771.

[75] H. Bae, S. Bae, C. Park, et al., "Digitally controlled wrinkle patterning," in *Proc. of The 20th International Conference on Miniaturized Systems for Chemistry and Life Sciences*, Dublin, Ireland, October 9-13, 2016, pp. 1053-1054.

국문 초록

주름은 마루와 골로 이루어진 지형적 구조로 사람의 피부나 과일의 껍질 등 자연계에 존재하는 생물체에서 어렵지 않게 발견할 수 있다. 오래 전부터 이러한 주름이 형성되는 원리를 규명하기 위해 서로 다른 물리적 특성을 가지는 여러 물질 시스템에서 이론적인 연구들이 진행되어왔다. 이론적 접근뿐 만 아니라 기존의 상하향식 리쏘그래피 기술을 이용해 만들어 내기 힘든 마이크로 또는 나노스케일의 복잡한 삼차원 구조물을 주름이 만들어지는 현상을 활용하여 하상향식 방식의 패터닝 기술로 만들고 이를 응용하고자 하는 공학적인 연구들도 활발하게 진행되어 왔다.

주름이 생기는 방식은 본질적으로 랜덤한 특성에 기반하기 때문에 링클링을 통해 패턴을 만들어내기 위해서는 랜덤한 주름 구조를 조절할 수 있는 방법들이 필요하다. 주름을 인공적으로 만들어 내기 위해서는 서로 다른 물리적 특성을 가지는 기판과 필름으로 이루어진 이중층 구조물이 필요한데, 이러한 기판과 필름에 특정한 패턴을 미리 만들어 놓거나 여기에 가해지는 압축 응력을 조절하는 등의 방식들을 활용하여 주름을 조절하는 기술들이 개발되어 왔다. 하지만 기존의 대부분 기술들은 개별적인 마루들을 원하는 방향과 모양으로 자유자재로 패터닝 하거나, 한 번에 서로 다른 패턴을 지닌 구조물들을 대량으로 만들어 내는 것을 동시에 할 수는 없었다. 본 논문에서는 미세입자 기판에

주름을 패터닝하는 새로운 플랫폼을 개발하여 이를 가능하도록 하고, 이 플랫폼을 활용한 새로운 어플리케이션을 제시하여 주름 패턴의 활용성을 높이고자 한다.

이를 위해서 먼저 폴리머를 코어로 하고 단단한 실리카 층을 셀로 하는 코어셀 형태의 미세입자를 만들고, 이를 건조과정을 통해 수축시켜 자발적으로 입자 표면에 주름을 만드는 공정 과정을 개발하였다. 이러한 제작 과정 중에 폴리머입자의 탄성계수, 실리카 층의 두께, 미세입자의 형태 등 주름 패턴을 조절할 수 있는 변수들을 동적으로 변경할 수 있기 때문에, 서로 다른 조건을 가지는 다양한 주름진 미세입자 구조물을 효율적으로 만들어 낼 수 있다.

기본적으로 위아래 면이 평평한 디스크 모양의 미세입자에 실리카 코팅을 하고 건조시키면 2 축 응력에 의해 랜덤한 형태의 마루 패턴이 만들어 지는데, 이 형상이 사람마다 가지고 있는 고유한 지문과 유사하다는 점에 착안하여 주름진 미세입자를 복제 불가능한 인공 지문으로서 위조방지용 태건트로 활용할 수 있음을 보였다. 전통적인 지문 인식 알고리즘을 이용하여 인공 지문의 인증 과정을 데모하였으며, 주름 패턴의 고유한 정도와 인공 지문의 내구성 등을 분석하여 실제 물건에 부착하여 활용 가능함을 증명하였다. 이를 통해 랜덤한 주름 패턴도 기능적으로 활용할 수 있다는 것을 입증하였다.

다음으로는 주름 패턴을 대략적으로 조절할 수 있는 방법으로, 미세입자의 외형이나 입자 사이즈 대비 주름 패턴 파장의 비율을 변형하여 랜덤한 정도를 조절하거나, 입자 내부에 구멍을 내어 그 주변에서 마루들의 방향성을 조절할 수

있음을 보였다. 더 나아가 폴리머 입자 합성시 표면에 아주 미세한 홈들을 미리 형성하여, 이를 통해 링클링 과정 동안 마루들이 생성될 수 있는 영역을 가이드 함으로써 패턴을 자유자재로 디자인 할 수 있는 정교한 주름 조절 방식을 개발하였다. 기존의 랜덤한 패턴을 형성하는 공정 과정에서 단지 폴리머 입자 합성 시 마스크 패턴만 바꿈으로써 마루들의 방향성을 개별적으로 정확하게 조절 할 수 있었다. 이 방식을 이용하여 입자 전체에 걸쳐 한 방향, 수직 방향, 그리고 육방으로 정렬된 주름 패턴을 가지는 구조물을 자가 조직화 하였으며, 더 나아가 글자 모양 등 임의의 패턴도 구현하였다.

이 논문에서는 폴리머 입자에 실리카 층이 씌워진 구조물만 활용하여 주름을 패터닝 하였지만, 개발된 주름을 조절하기 위한 접근 방식들은 다른 물질이나 형태로 이루어진 구조물에도 적용될 수 있을 것으로 보인다. 또한 개발된 미세입자 기반의 조절 가능한 주름 패터닝 기술과 이를 이용해 만든 구조물들은 기계적 불안정성을 연구하기 위한 플랫폼 등 이 논문에서 제시된 것 외에도 다양한 곳에 활용될 수 있을 것으로 기대한다.

주요어 : 주름 패터닝, 주름 조절, 미세입자, 위조방지, 자가 조직화

학번 : 2013-30238